Fall 2007

Empirical dynamic modeling and nonlinear force control of friction stir welding

Xin Zhao

Follow this and additional works at: https://scholarsmine.mst.edu/masters_theses

Part of the Mechanical Engineering Commons

Department:

Recommended Citation

EMPIRICAL DYNAMIC MODELING AND

NONLINEAR FORCE CONTROL OF FRICTION STIR WELDING

by

XIN ZHAO

A THESIS

Presented to the Faculty of the Graduate School of the

UNIVERSITY OF MISSOURI-ROLLA

In Partial Fulfillment of the Requirements for the Degree

MASTER OF SCIENCE IN MECHANICAL ENGINEERING

2007

Approved by

_____   _____
Dr. Robert G. Landers, Advisor   Dr. K. Krishnamurthy

_____
Dr. Rajiv S. Mishra

PUBLICATION THESIS OPTION

This thesis consists of the following two articles that have been submitted for publication as follows:

Pages 3–38 were submitted and accepted to the ASME International Conference on Manufacturing Science and Engineering, Atlanta, Georgia, October 15–18, 2007.

Pages 39–85 are intended for submission to the ASME Journal of Manufacturing Science and Engineering.

ABSTRACT

Current Friction Stir Welding (FSW) process models are mainly concerned with the detailed analysis of material flow, heat generation, etc. and therefore, are computationally intensive. Dynamic models describing the total forces acting on the tool throughout the entire welding process are required for the design of feedback control strategies and improved process planning and analysis. In this thesis, empirical models relating the process parameters (i.e., plunge depth, travel speed, and rotation speed) to the process variables (i.e., axial, path, and normal forces) are developed to describe their dynamic relationships. First, the steady–state relationships are constructed, and next, the dynamic characteristics of the process variables are determined using Recursive Least Squares. The steady–state relationship between the process parameters and process variables is well characterized by a nonlinear power relationship, and the dynamic responses are well characterized by low–order linear equations. Experiments are conducted to validate these models.

Subsequently, this thesis presents the systematic design and implementation of nonlinear feedback controllers for the axial and path forces of FSW processes, based on the dynamic process and equipment models. The controller design uses the Polynomial Pole Placement (PPP) technique and the controllers are implemented in a Smith–Predictor–Corrector (SPC) structure to compensate for the inherent equipment delay. In the axial force controller implementation, a constant axial force is tracked, both in lap welding and welding along or across gaps. In the path force controller implementation, a constant path force is tracked and surface and internal defects generation during the welding process is eliminated by regulating the path force.

ACKNOWLEDGMENTS

TABLE OF CONTENTS

LIST OF ILLUSTRATIONS

LIST OF TABLES

SECTION

1. INTRODUCTION

Friction Stir Welding (FSW), a solid–state welding technology, was invented and patented by The Welding Institute (TWI, UK) in 1991, and is finding increased applications in many industries including aerospace, automobile, marine and land transportation. In FSW processes, a non–consumable tool, consisting of a pin with a smaller diameter and a broader shoulder, rotates and plunges into the parts to be joined such that both the pin and the shoulder are in contact with the part surface. The tool rotation induces material plastic deformation and, after a certain time of dwelling, the tool travels along, or across the intersection of the parts. The parts are joined together as the tool leaves the processing zone. This technique has advantages in that it can weld high strength materials (e.g., the 2000 and 7000 series aluminum alloys) that are difficult to weld by conventional welding processes, part distortion and residual stresses are low, and joint strength is high. Moreover, the FSW process is environmentally friendly because no harmful fumes or gases are generated during the operation.

The FSW process involves complex material flow dynamics, thermo–mechanical coupling dynamics, and metallurgical changes. The process outputs, including dynamic variables (e.g., axial, path, and normal forces), material mechanical properties, and the temperature distribution in the welding zone, depend on several factors including tool features and geometry, process parameters (e.g., plunge depth, tool travel rate, tool rotation speed, tool work and travel angles), fixturing, and the thermo–mechanical properties of the materials to be joined. Most of the current FSW process modeling

research work is concerned with material flow and temperature distribution during the process and finite element and finite difference methods are typically used to solve the complex governing partial differential equations. Therefore, these models are significantly limited in real–time control applications due to their heavy computational burden. Empirical dynamic models, presented in the first paper, is an attempt to describe the total forces acting on the tool during the entire process by modeling the dynamic characteristics of the forces, and can be used for process planning, analysis, and especially for the design of real–time feedback controllers.

The dynamic force models provide the bases for the design of FSW force controllers. Force control strategies are significantly important for FSW processes in that 1) an axial force control mechanism is necessary to achieve a quality weld due to the existence of material manufacturing errors, gaps between plates, improper fixturing, and plunge depth variation due to the machine structural deformation and 2) defects such as surface and internal voids can be eliminated by the implementation of a path force controller to regulate the path force. Based on the dynamic models, the design and implementation of nonlinear axial and path force controllers on a robotic FSW system are presented in the second paper. Also, various validation experiments are conducted to verify the controllers' performance.

PAPER

I: Empirical Dynamic Modeling of Friction Stir Welding Processes

Xin Zhao, Prabhanjana Kalya, Robert G. Landers, and K. Krishnamurthy

University of Missouri–Rolla, Mechanical and Aerospace Engineering Department

1870 Miner Circle, Rolla, Missouri 65409–0050, USA

{xzvc8;pk34b;landersr;kkrishna}@umr.edu

Abstract

Current Friction Stir Welding (FSW) process modeling research is mainly concerned with the detailed analysis of local effects such as material flow, heat generation, etc. These detailed thermo–mechanical models are typically solved using finite element or finite difference schemes and require substantial computational effort to determine temperature, forces, etc. at a single point in time, or for a very short time range. Dynamic models describing the total forces acting on the tool throughout the entire welding process are required for the design of feedback control strategies and improved process planning and analysis. In this paper, empirical models relating the process parameters (i.e., plunge depth, travel speed, and rotation speed) to the process variables (i.e., axial, path, and normal forces) are developed to understand their dynamic relationships. First, the steady–state relationships between the process parameters and process variables are constructed, and the relative importance of each process parameter on each process variable is determined. Next, the dynamic characteristics of the process variables are determined using Recursive Least Squares. The results indicate the steady–state

relationship between the process parameters and process variables is well characterized by a nonlinear power relationship, and the dynamic responses are well characterized by low–order linear equations. Experiments are conducted that validate the developed FSW dynamic models.

Key words: friction stir welding, dynamic process modeling, least squares, recursive least squares

Nomenclature

d plunge depth (mm)

F_f general filtered force (kN)

F_m general measured force (kN)

F_x path force (kN)

F_y normal force (kN)

F_z axial force (kN)

v travel speed (mm/s)

ρ relative deviation

ρ_{con} relative deviation in experiments where process parameters are constant

ρ_{step} relative deviation in experiments where process parameters are changed stepwise

$\rho_{\sin}$ relative deviation in experiments where process parameters are changed sinusoidally

ω rotation speed (rpm)

1. Introduction

Friction Stir Welding (FSW) is a solid state welding technology that has been used successfully in many joining applications [1]. In the FSW process, a rotating non–consumable tool, consisting of a pin and shoulder, plunges into a part such that both the pin and shoulder are in contact with the part. The tool rotation induces gross material plastic deformation due to an elevated temperature field. After dwelling for a period of time, the tool travels along the intersection of two parts, joining them as the tool leaves the processing zone. The FSW process has advantages in that it can weld materials (e.g., 2XXX and 7XXX aluminum alloys) that are difficult to weld by conventional welding techniques, and part distortion and residual stresses after welding are low. Also, the FSW process is environmentally friendly since no harmful gases are generated during the operation. A schematic of a FSW process where two plates are being lap welded is shown in Figure 1.

The FSW process is a complex physical phenomenon, involving material flow dynamics, thermo–mechanical coupling dynamics, and metallurgical changes. The process outputs include dynamic variables (e.g., axial, path, and normal forces), mechanical properties of the welded materials, and the temporal and spatial temperature distribution in the welding zone. These outputs depend on several factors including tool geometry, process parameters (e.g., plunge depth, travel speed, rotation speed, tool work and travel angles), fixturing, and the thermo–mechanical properties of the materials to be joined. Most of the current FSW process modeling research work is concerned with two–dimensional and three–dimensional material flow and temperature distribution in the heat affected, thermo–mechanical affected, and stir zones. Due to the complexity of the

governing partial differential equations, finite element and finite difference methods are typically used in these research studies.

Deng and Xu [2] developed a three–dimensional finite element simulation of the FSW process that focused on simulating the velocity field, material flow, and plastic strain distribution. The authors compared their predicted results to experimental data and observed a reasonable correlation between the equivalent strain distribution and observed micro–structural features. However, their finite element analysis was not a thermo–mechanical coupled procedure, which affected the welding force prediction. Ulysse [3] presented a three–dimensional finite element visco–plastic model for FSW of thick aluminum plates using the finite element code FIDAP, a commercial fluid dynamic analysis package. The author investigated the effect of travel speed and rotation speed on the process output variables. It was found that higher travel speeds lead to higher welding forces, while increasing the rotation speed had the opposite affect. Chen and Kovacevic [4] developed a three–dimensional finite element model to study the thermo–mechanical phenomena in the friction stir butt–welding process of a 6061–T6 aluminum alloy. Their model incorporated the mechanical reaction between the tool and the weld material. Measurements of the forces were presented and revealed a reasonable agreement between the experimental results and numerical calculations. Colegrove and Shercliff [5] used a commercial Computational Fluid Dynamics (CFD) software package for two–dimensional and three–dimensional numerical investigations on the influence of pin geometry, and good results were obtained. Heurtier et al. [6] presented a semi–analytical three–dimensional thermo–mechanical model and used it to predict strains, strain rates, temperatures, and hardness in the weld zone. The calculated and measured results were in

good agreement. Zhang et al. [7] presented a model of FSW processes that incorporated rate dependent (i.e., history functional type) constitutive material laws. The finite element method was used to conduct simulation studies. Vilaca et al. [8] demonstrated the feasibility of using the analytical thermal code iSTIR to model the FSW process. The heat power dissipated during the steady–state portion of the welding process was calculated and correlations between the thermal efficiency and FSW process parameters were established. Kalya et al. [9] constructed a temperature mechanistic model for process specific energy and surface temperature profile of the work material and obtained good estimation results. Boldsaikhan et al. [10] studied the phase space trajectory of the normal force in FSW processes of a 7075 aluminum alloy, using it evaluate weld quality. Lyapunov exponents and a Poincaré map were used to quantify the stability of the dynamic system and promising results were shown for both methods. Arbegast [11] reviewed several techniques used in Statistical Process Control and feedback control for FSW processes, and compared their efficiency, precision, and limitations. Statistical correlations were made between process parameters and process forces.

Despite the advances in FSW process modeling research, most of the models are numerically intensive. This heavy computational burden severely limits their applications in the real–time control of process variables since computational efficiency is required. Therefore, an empirical dynamic model, which is able to describe the dynamic characteristics of the welding process with adequate precision, is critical for the design of feedback control strategies. Moreover, dynamic models that describe the input–output characteristics of FSW processes can also be used for process planning and analysis.

The rest of this paper is organized as follows. First, the setup used for the experimental studies conducted in this paper is described. Then, dynamic models of the FSW process that take the process parameters (i.e., plunge depth, travel speed, and rotation speed) as inputs and the process variables (i.e., axial, path, and normal forces) as outputs are created in two steps. First, nonlinear static relationships are derived and the importance of each process parameter on each process variable is evaluated. Next, the dynamic relationships are determined. Lastly, the experimental validation of these dynamic models is conducted and analyzed.

2. Experimental Setup

A 6061–T6 aluminum alloy is used as the weld material for the experimental studies conducted in this paper. The detailed composition (by weight) of this aluminum alloy is: 97.9% Al, 0.60% Si, 0.3% Cu, 1.0% Mg, and 0.20% Cr. The tool is tapered, threaded, and contains three flats. The FSW system (Figure 2) consists of a six degree of freedom robot, a FSW spindle head, a six–axis force/moment sensor, and a control system that is open at the high programming levels. The robot is an IRB 940 Tricept robot from ABB, Inc. with three non parallel telescopic translational joints and three rotational joints. A teach pendant allows the user to manually control and program the robot. The robot is retrofitted with a FSW spindle head that provides the rotational tool motion.

The FSW spindle head (Figure 3) consists of a rotational axis driven by an external 10 hp Exlar SLM115–368 servo motor with a rotational speed range of ±3000 rpm. The controller and drives are placed in the control housing. The load capability of

the spindle is rated up to 9 kN (2,023 lb) along the tool axis and 4.5 kN (1,012 lb) in the radial direction. The six–axis force/moment sensor system (model 75E20S–M125A–A 6000N1150 from JR3 Inc.) provides measurements of the forces acting in three orthogonal directions, as well as moments about each of these directions. The outputs are analog voltage signals with ranges of ±10.0 V. The rated forces for the sensor are 6 kN (1,348 lb) in the radial direction and 12 kN (2,696 lb) in the axial direction. The rated moments are 1,150 N·m (848 ft·lb) about all three directions.

The IRB 940 Tricept robot uses an S4cPlus robot control unit with RAPID as the programming language. As a high level language, RAPID enables the operator to pre–program the processing sequence and control algorithms in a textual format, upload the source program to the robot's control unit, and compile and execute the code. Figure 4 shows the basic structure and function blocks of the program. As shown in Figure 4, the main body of the code contains a loop, which executes in real–time during the welding process, between the initialization and data storage routines. An interrupt procedure with a period of 0.1 sec is triggered before entering the main welding loop in order to provide a constant frequency of data acquisition and commanded process parameter output. During the interrupt procedure, the sensor signals (i.e., measured axial, path, and normal forces and measured process parameters) are collected and output signals (i.e., commanded process parameters) are calculated. These data are sent to the main loop where the sensor data is stored and the output signals are sent to their respective amplifiers. After the main loop finishes, all collected data are saved to the control unit hard disk and, thus, are available for analysis at a later time (see Figure 5).

The measured force data contains significant noise mainly due to electrical noise in the control unit. Therefore, a moving average algorithm is applied to the measured force data to filter the noise. A five–point moving average was empirically determined to provide good force data filtering without significant signal delay and unduly taxing the system's limited computational bandwidth. The filtered force signal is

$$F_f\left(i\right)=\frac{1}{5}\left(F_m\left(i\right)+F_m\left(i-1\right)+F_m\left(i-2\right)+F_m\left(i-3\right)+F_m\left(i-4\right)\right) \tag{1}$$

where $F_f\left(i\right)$ is the filtered force data at the ith iteration and $F_m\left(i\right)$ is the measured force data at the ith iteration. Figure 6 shows the comparison of the measured and filtered force data during a constant process parameter welding experiment. The standard deviations of the measured and filtered force data are 0.062 *kN* and 0.031 *kN*, respectively; thus, a decrease of 50% is realized.

3. Dynamic Process Modeling

The FSW process is a complex thermo–mechanical process that is affected by many factors such as plunge depth, travel speed, rotation speed, fixturing, material thermo–mechanical properties, tool geometry, etc. In this study, the process parameters include plunge depth, travel speed, and rotation speed, and the process variables include axial (Z), path (X), and normal (Y) forces acting on the tool, as shown in Figure 7. Due to the complexity of FSW process, the process variables are significantly affected by factors other than the process parameters. These factors include fixturing, weld material properties, tool geometry, work and travel angles, etc. However, for the studies conducted in this paper, these factors were constant; therefore, they are not considered as

input parameters. In this paper, dynamic models of the process variables, taking the process parameters as the inputs, are created and discussed.

The parameter ranges were selected such that surface voids were not observed and equipment constraints were not violated (e.g., there is a minimum plunge depth such that the tool shoulder maintains contact with the plate's surface). The process parameter ranges selected for the studies conducted in this paper are: 2.0 mm/s $\leq v \leq$ 3.2 mm/s, 1600 rpm $\leq \omega \leq$ 2100 rpm, and 4.191 mm $\leq d \leq$ 4.445 mm. It should be noted that plunge depth is zero when the bottom of the pin is touching the top surface of the top plate. The plates were cut and 5 mm sections around the nugget were encased in an epoxy, ground and polished several times using increasing fine grit sizes, and etched with acid to visually examine the cross sections of the weld region. Neither surface nor internal voids were detected; however, several nuggets had hooking defects as shown in Figure 8. Also, some combinations of process parameters produced flash (i.e., material that leaves the sides of the processing zone).

3.1 Experimental Design

A series of welding experiments were conducted to gather both steady–state and dynamic response data. Three groups, each consisting of nine experiments, were designed. For each group, two of the process parameters were constant. During each experiment, one process parameter changed in a step–wise manner four times (twice increasing and twice decreasing) between three levels. The process parameter data for groups 1, 2, and 3 are given in Tables 1, 2, and 3, respectively.

12

3.2 Axial Force

The axial force in FSW processes is caused by the pressure acting on the end of the tool's pin and shoulder. This creates a forging action that produces good part microstructure. The axial force has the largest magnitude among the three force components for the FSW operations considered in this paper. Creating the axial force process model consists of two steps: static modeling and dynamic modeling. Figure 9 shows typical axial force responses during experiments with individual step changes in the three process parameters. An increase in both plunge depth and travel speed results in an increase in the axial force and an increase of rotation speed results in a decrease in the axial force.

In each experiment, one process parameter changes in a step–wise manner four times. The duration of each change is long enough for the forces to reach a steady–state. Therefore, taking the average axial force and process parameters during the steady–state portion of the 27 experiments, 135 steady–state data sets are obtained. The following model is used to describe the static relationship between the axial force and process parameters

$$F_z = K d^\alpha v^\beta \omega^\lambda \tag{2}$$

This nonlinear power model has been successfully used to characterize torque in friction stir welding processes [9]. Taking the natural log of equation (2)

$$y = K_e + \alpha x_1 + \beta x_2 + \gamma x_3 \tag{3}$$

where $y = \ln(F_z)$, $x_1 = \ln(d)$, $x_2 = \ln(v)$, $x_3 = \ln(\omega)$, and $K_e = \ln(K)$. The output variable y has a linear relationship with the input parameters x_1, x_2, and x_3; therefore, this model is built and evaluated using linear regression analysis. The unknown parameters α, β, γ, and

K_e can be estimated using the Least Squares (LS) method. The resulting static axial force model is

$$F_z = 0.131 d^{2.207} v^{0.097} \omega^{-0.230} \tag{4}$$

The correlation coefficient is 0.871 and the standard deviation is 0.109 kN, indicating a good model. The T–ratios of the input parameters (i.e., x_1, x_2, x_3) are calculated in order to evaluate their statistical significance [12], and are 17.3, 6.12, and 8.51, respectively. For a data set containing more than 120 observations, a T–ratio is 1.658 indicates a probability of less than 10% that the corresponding input parameter is statistically significance. Therefore, based on the T–ratios, all three input parameters are statistically significance. The relationship between the modeled and measured steady–state axial force is shown in Figure 10.

To evaluate the relative importance of each input parameter in the static model, standardization is applied [12]. Denoting $\bar{y}$, $\bar{x}_1$, $\bar{x}_2$, and $\bar{x}_3$ as the average values of y, x_1, x_2, and x_3, respectively, and $\sigma(y)$, $\sigma(x_1)$, $\sigma(x_2)$, and $\sigma(x_3)$ as the standard deviation of y, x_1, x_2, and x_3, respectively, the standardized output variable y_s and input parameters x_{1s}, x_{2s}, and x_{3s}, respectively, are

$$y_s = \frac{y - \bar{y}}{\sigma(y)} \tag{5}$$

$$x_{1s} = \frac{x_1 - \bar{x}_1}{\sigma(x_1)} \tag{6}$$

$$x_{2s} = \frac{x_2 - \bar{x}_2}{\sigma(x_2)} \tag{7}$$

$$x_{3s} = \frac{x_3 - \bar{x}_3}{\sigma(x_3)} \tag{8}$$

The relationship between the standardized output variable and the input parameters is expressed as

$$y_s = \alpha_s x_{1s} + \beta_s x_{2s} + \gamma_s x_{3s} \tag{9}$$

where α_s, β_s, and γ_s are standardized coefficients. By using the LS method, the standardized coefficients are $\alpha_s = 0.745$, $\beta_s = 0.263$, and $\gamma_s = -0.365$. The standardized coefficient magnitudes represent the relative importance of the corresponding process parameters. The magnitudes of β_s and γ_s are significantly less than the magnitude of α_s. Therefore, within the process parameter ranges considered in these studies, the plunge depth has the dominant influence on the axial force.

In the static model it is seen that the plunge depth has the greatest influence on the axial force. In addition, the axial force dynamic response did not show a consistent pattern when the travel speed and tool rotational speed changed in a step–wise manner (see Figures 11 and 12). The axial force sometimes decreased when the travel speed or rotation speed were constant and sometimes did not change when these process parameters increased or decreased. Therefore, a dynamic axial force process model is now constructed with only the plunge depth as the input. Typical experimental results (see Figure 9) show overshoot during the transient phase of the dynamic response. Given this response and the static model developed above, the following second order discrete time model is proposed

$$F_z(z) = v^{0.097} \omega^{-0.230} \frac{b_1 z + b_0}{z^2 + a_1 z + a_0} d^{2.207}(z) \tag{10}$$

where b_0, b_1, a_0, and a_1 are unknown model coefficients to be determined.

To estimate these coefficients, equation (10) is converted into the following difference equation

$$\frac{F_z(k)}{v^{0.097}\omega^{-0.230}} = -a_1 \frac{F_z(k-1)}{v^{0.097}\omega^{-0.230}} - a_0 \frac{F_z(k-2)}{v^{0.097}\omega^{-0.230}} + b_1 d^{2.207}(k-1) + b_0 d^{2.207}(k-2) \quad (11)$$

and the model parameters are estimated using the Recursive Least Squares (RLS) method for each experiment in Group 1. Then equation (10) is converted into

$$F_z(s) = \frac{Kv^{0.097}\omega^{-0.230}(s-b)}{(s-p_1)(s-p_2)} d^{2.207}(s) \quad (12)$$

using the Matlab function **d2c** (discrete to continuous) where b, p_1, p_2, and $-Kb/(p_1 \cdot p_2)$ are the transfer function zero, poles, and steady–state gain, respectively. Table 4 shows the model parameters, as well as their averages, for the nine experiments in Group 1.

It is noted that the results of the fifth experiment are quite different from the other experiments; therefore, this experiment is treated as an outlier and not used to compute the average model parameter values. The dynamic process model in the continuous time domain is constructed based on the average values of the model parameters and is

$$\begin{aligned} F_z(s) &= \frac{3.86v^{0.097}\omega^{-0.230}(s+2.25)}{(s+25.5)(s+2.65)} d^{2.207}(s) \\ &= v^{0.097}\omega^{-0.230}\left(\frac{3.82}{s+25.5} + \frac{-0.0658}{s+2.65}\right) d^{2.208}(s) \end{aligned} \quad (13)$$

The process contains two distinct modes: one with a positive gain and a fast speed of response and one with a negative gain and a slow speed of response. Mathematically, this explains why overshoot is present even though both poles are over damped. Physically, the two modes may represent the effects of thermo–mechanical processes. Also, these modes may be influenced by the machine's dynamic structural characteristics.

3.3 Path Force

The path force is the force imposed on the tool along the welding direction. There are two main effects that produce the path force. First, in the plastic deformation zone the material is being stirred and there is an imbalance from the leading to the trailing edge that causes a net path force. Second, the plastic deformation zone is moving toward unprocessed material, which causes a reaction force on the tool in the path direction. By utilizing similar procedures as were implemented in modeling the axial force, the path force dynamic model is created. The LS method is applied to the 135 steady–state data sets to develop a nonlinear static path force model with a similar structure to that of equation (2). The correlation coefficient for this model is 0.781, indicating only a fair model. The path force data had significantly more variation than the axial force data. This is due to the fact that the stirring process is more chaotic than the forging process. Due to the significant variation in the data, Chevenout's criterion was applied. Every data set that fell outside of three standard deviations of the model was removed from the experimental data and a new path force model was created. The procedure was repeated until all the remaining data sets were within three standard deviations. After applying Chevenout's criterion, 134 data sets are used yielding the following path force static model

$$F_x = 0.704d^{-1.054}v^{0.999}\omega^{-1.236} \tag{14}$$

The correlation coefficient is 0.789 and the standard deviation is 0.035 kN. The T–ratio of each process parameter is then calculated to evaluate their statistical significance. The T–ratios of the plunge depth, travel speed, and rotation speed are 1.55, 11.8, and 8.58, respectively. The T–ratio corresponding to the plunge depth shows that the probability is

less than 10% that it is statistically significance in the path force model. This indicates that the influence of the plunge depth on the path force is negligible, as compared to the influence of the travel speed and rotation speed, within the process parameter ranges utilized in these studies. Therefore, the following static model is proposed

$$F_x = K v^\beta \omega^\lambda \tag{15}$$

The unknown coefficients are estimated using the LS method and the resulting model is

$$F_x = 0.151 v^{0.999} \omega^{-1.23} \tag{16}$$

The relationship between the modeled and measured path force for the 134 data sets is shown in Figure 13. The correlation coefficient is 0.784 and the standard deviation is 0.036 kN. The low correlation coefficient, as compared to that of the axial force model, indicates the path force model has much greater variation than the axial force model. This is due to the fact that the path force magnitude (approximately 0.1–0.4 kN) is an order of magnitude lower than the axial force magnitude (approximately 2.0–4.0 kN) and, thus, the influence of the electrical noise, fixturing variations, etc. is greater. Also, this indicates that the stirring process is more chaotic than the forging process.

The standardized regression coefficients are $\beta_s = 0.637$ and $\gamma_s = -0.461$, indicating that, for the path force, the travel speed is slightly more significant than the rotation speed. While the correlation coefficient for the static path force model is only fair, the model still reveals the influence of the process parameters on the path force: an increase in the travel speed results in an increase in the path force and an increase in the rotation speed results in a decrease in the path force.

Due to the dominant affect of the travel speed and rotation speed on the path force, a dynamic model with both of these process parameters as the inputs is

constructed. The data show that the dynamic responses are over damped and well–characterized by first order linear models. However, the data also show that for the path force, significant uncertainties and nonlinearities exist during the welding process. For example, it can be seen in Figure 14 that the path force sometimes did not change when the process parameters changed, and the path force sometimes changed when the process parameters were constant.

The time constants for the data with travel speed step changes (i.e., Group 2) and the data with rotation speed step changes (i.e., Group 3) were computed, using only transient responses that noticeably changed when the process parameters changed (see Figure 15) and that had the same steady–state relationship as the static model in equation (16). For Groups 2 and 3, seven and fourteen transient states, respectively, met these criteria. The RLS method is implemented to determine the time constants for the twenty–one transient states. For the seven transient states from Group 2, the time constants are 0.491, 0.721, 0.640, 0.976, 0.560, 0.329, and 0.0943 sec, with an average time constant of 0.539 sec and corresponding standard deviation of 0.288 sec. For the fourteen transient states from Group 3, the time constants are 1.13, 1.47, 0.259, 0.325, 0.970, 1.64, 0.626, 0.131, 0.531, 0.478, 0.0545, 0.361, 0.963 and 0.631 sec, with an average time constant of 0.684 sec and corresponding standard deviation of 0.487 sec.

The large variation in the computed time constants and the fact that not all of the responses exhibited the expected behavior are due to the chaotic behavior of the stirring process. However, the average time constants based on Group 2 and Group 3 data are similar: 0.539 and 0.684 sec, respectively.

The following dynamic path force model is proposed based on the weighted average of the twenty–one time constants

$$F_x(s) = \frac{0.151}{0.635s+1}\left(v^{0.999}\omega^{-1.232}\right)(s) \tag{17}$$

Note that the input parameter is the product of the travel speed and rotation speed, and the time constant is the weighted average of the time constants computed for Groups 2 and 3 data. The physical explanation for the first order effect is probably due to thermo–mechanical transient effects in the region of plastic material flow and the machine's dynamic structural characteristics.

3.4 Normal Force

The normal force is the force imposed on the tool in the plane of the part and perpendicular to the path direction. This force is typically directed from the weld retreating side to the weld advancing side and is caused by the unbalance of the material flow on the two sides. The same modeling procedure used to construct the path force model is applied to construct the normal force model. Chevenout's criterion is applied to the steady–state data sets and 133 data sets are used to construct the static normal force model

$$F_y = 20.8d^{-3.93}v^{0.654}\omega^{-0.277} \tag{18}$$

The correlation coefficient is 0.639 and the standard deviation is 0.030 kN, indicating a poor model. The T–ratios are calculated for the plunge depth, travel speed, and tool rotational speed and are 5.54, 7.39, and 1.83, respectively. The standardized regression coefficients are $\alpha_s = -0.375$, $\beta_s = 0.500$, and $\gamma_s = -0.124$, indicating that for the normal

force the travel speed has the most significant affect. The relationship between the modeled and measured normal forces is shown in Figure 16.

While both the travel speed and plunge depth have a significant influence on the normal force, for the dynamic model only the travel speed is taken as the input since the normal force dynamic response with respect to the plunge depth did not show a consistent pattern. Figure 17 shows normal force responses for experiments where the plunge depth was changed in a step–wise manner. In these experiments the normal force sometimes increased and sometimes decreased when the plunge depth increased, the normal force did not show an obvious change in some experiments when the plunge depth changed, and a consistent transient behavior in the normal force was not observed in the Group 1 experiments. However, twelve normal force transient responses in the Group 2 experiments showed the expected responses (see Figure 18 as an example) to step changes in the travel speed and, therefore, were selected to construct dynamic models. It was noted that the responses were over damped and well characterized by a first order dynamic model; therefore, RLS was used to determine the time constants for the twelve data sets in the Group 2 experiments. The time constants are 0.456, 0.592, 0.431, 0.253, 0.319, 0.711, 0.275, 0.437, 0.450, 0.241, 0.343, and 0.549 sec. The average time constant is 0.421 sec, and the standard deviation is 0.145 sec.

Using the average time constant, the normal force dynamic model is

$$F_y(s) = \frac{20.8d^{-3.93}\omega^{-0.277}}{0.421s+1}v^{0.654}(s) \tag{19}$$

The low correlation coefficient of the static normal force model and the inconsistencies in the transient responses are due to the chaotic behavior of the stirring process. Again, the physical explanation for the first order effect is probably due to thermo–mechanical

transient effects in the region of plastic material flow and the machine's dynamic structural characteristics.

4. Model Validation

Validation experiments are conducted to evaluate the accuracy of the FSW force models created above. The deviations between the modeled and measured forces were calculated and compared to the standard deviation of forces in an experiment where the process parameters remained constant to evaluate the accuracy of the models.

4.1 Axial Force

Figure 19 shows a comparison of the modeled and measured axial force during an experiment where the plunge depth was changed in a step–wise manner. The axial force standard deviation between the modeled and measured values is 67.8 N for this experiment. Figure 20 shows a comparison of the modeled and measured axial force for an experiment where the plunge depth was changed sinusoidally with an amplitude and frequency of 0.4 mm and 0.1 Hz, respectively. The axial force standard deviation between the modeled and measured values is 139 N for this experiment. Both experiments validate the axial force dynamic model.

4.2 Path Force

According to equation (17), travel speed and rotation speed are the input process parameters for the path force dynamic model. Therefore, the validation experiments

consisted of the following two scenarios: plunge depth is constant and 1) travel speed and rotation speed are changed simultaneously using different combinations of constant values and 2) travel speed and rotation speed are changed simultaneously using sinusoidal profiles. The measured and modeled path force and process parameter profiles for scenarios 1 and 2 are shown in Figure 21. The standard deviations between the measured and modeled forces in scenarios 1 and 2 are 29.7 and 35.2 N, respectively, indicating a good path force model.

4.3 Normal Force

The normal force validation experiments are similar to those used to validate the path force model. Keeping the plunge depth constant, two scenarios are considered: 1) travel speed and rotation speed are changed simultaneously using different combinations of constant values and 2) travel speed and rotation speed are changed simultaneously using sinusoidal profiles. The measured and modeled normal force and the process parameter profiles for scenarios 1 and 2 are shown in Figure 22. The standard deviations between the measured and modeled forces for scenarios 1 and 2 are 25.2 N and 24.7 N, respectively, indicating a good normal force model.

To further quantify the accuracy of the dynamic models, the relative deviation between the modeled and measured data is considered. A variable ρ is defined as the relative deviation, i.e., the ratio of the standard deviation between the modeled and measured process variables during an experiment to the average of the measured process variable during the experiment. For each process variable two values of ρ are computed: ρ_{step} for the validation experiment where one or two process parameters were changed in

a step–wise manner and ρ_{sin} for the validation experiment where one or two process parameters were changed sinusoidally. As a comparison, the relative deviation of the process variables, referred to as ρ_{con}, is computed for an experiment where the process parameters remained constant ($d = 4.191$ mm, $v = 2.6$ mm/s, and $\omega = 1450$ rpm). Table 6 shows the relative deviations for the validation experiments and the experiment with constant process parameters. From Figures 18–22 and Table 5, it can be seen that the dynamic force models fit the experimental data very well.

5. Summary and Conclusions

The process variables (i.e., axial, path, and normal forces) in a FSW process were dynamically modeled as functions of the process parameters (i.e., plunge depth, travel speed, and rotation speed). The modeling procedure consisted of two steps: static modeling using the LS method and dynamic modeling using the RLS method. To the authors' knowledge this is one of the very first studies to investigate the dynamics of the FSW process.

According to the experimental results, the axial force is primarily affected by the plunge depth and may be modeled as a second order dynamic process with two real poles. The axial force process does, however, contain overshoot since the zero is close to a pole. The path force is primarily affected by the travel speed and rotation speed and may be modeled as a first order process. The normal force is affected by all three process parameters and may also be modeled as a first order process. It is believed that the mechanical and thermal processes, as well as the machine's dynamic structural

characteristics, affect the dynamic response of the forces; however, further investigation is required. The static axial force model correlation coefficient was very good. The static path and normal force models had fair and poor correlation coefficients, respectively. The reason these two models were not as good as the axial force model is believed to be due to the chaotic behavior of the stirring process, as compared to the forging process, and the smaller signal to noise ratio. Various validation experiments were conducted and validated the accuracy of the developed models.

6. Acknowledgements

7. References

[1]   Mishra, R.S. and Ma, Z.Y., 2005, "Friction Stir Welding and Processing," *Materials Science and Engineering: R*, Vol. 50, No. 1–2, pp. 1–78.

[2]   Deng, X. and Xu, S., 2001, "Finite Element Simulation of the Friction Stir Welding Process," *USACM: Sixth US National Congress on Computational Mechanics Abstracts*, Dearborn, Michigan, August 1–3, p. 201.

[3] Ulysse, P., 2002, "Three–Dimensional Modeling of the Friction Stir Welding Process," *International Journal of Machine Tools and Manufacture*, Vol. 42, No. 14, pp. 1549–1557.

[4] Chen, C. and Kovacevic, R., 2004, "Thermo–Mechanical Modeling and Force Analysis of Friction Stir Welding by the Finite Element Method," *Proceedings of the Institution of Mechanical Engineers C, Journal of Mechanical Engineering Science*, Vol. 218, No. C5, pp. 509–519.

[5] Colegrove, P.A. and Shercliff, H.R., 2005, "3–Dimensional CFD Modeling of Flow Round a Threaded Friction Stir Welding Tool Profile," *Journal of Materials Processing Technology*, Vol. 169, No. 2, pp. 320–327.

[6] Heurtier, P., Jones, M., Desrayaud, C., Driver, J., Montheillet, F., and Allehaux, D., 2006, "Mechanical and Thermal Modeling of Friction Stir Welding," *Journal of Materials Processing Technology*, Vol. 171, No. 3, pp. 348–357.

[7] Zhang H. and Zhang Z., 2007, "Numerical Modeling of Friction Stir Welding Process by using Rate–Dependent Constitutive Model," *Journal of Materials Science and Technology*, Vol. 23, No. 1, pp. 73–80.

[8] Vilaca, P., Quintino, L., dos Santos, J., Zettler, R., and Sheikhi, S., 2007, "Quality Assessment of Friction Stir Welding Joints via an Analytical Thermal Model, iSTIR," *Materials Science and Engineering: A – Structural Materials: Properties, Microstructure and Processing*, Vol. 445–446, pp. 501–508.

[9]   Kalya, P., Krishnamurthy, K., Mishra, R.S., and Baumann, J.A., 2007, "Specific Energy and Temperature Mechanistic Models for Friction Stir Processing of Al–F357," Mishra, R.S. *et al*., eds., *Symposium on Friction Stir Welding and Processing IV*, TMS Annual Meeting and Exhibition, Orlando, Florida.

[10]   Boldsaikhan, E., Corwin, W., Logar, A., McGough, J., and Arbegast, W., 2007, "Phase Space Analysis of Friction Stir Weld Quality," *Friction Stir Welding and Processing IV*, pp. 101–112.

[11]   Arbegast, W., 2005, "Using Process Forces as a Statistical Process Control Tool for Friction Stir Welds," *Friction Stir Welding and Processing III*, San Francisco, California, February, pp. 193–204.

[12]   Montgomery, D.C. and Peck, E.A., 1992, *Introduction to Linear Regression Analysis*, 2nd ed., Wiley–Interscience, New York, New York.

Table 1: Constant Process Parameters for Group 1 Experiments. Plunge Depth is 4.191 mm for 10 sec, 4.318 mm for 10 sec, 4.445 mm for 10 sec, 4.318 mm for 10 sec, and 4.191 mm for 10 sec.

Experiment	1	2	3	4	5	6	7	8	9
v (mm/s)	2.0	2.0	2.0	2.6	2.6	2.6	3.2	3.2	3.2
ω (rpm)	1600	1900	2100	1600	1900	2100	1600	1900	2100

Table 2: Constant Process Parameters for Group 2 Experiments. Travel speed is 2.0 mm/s for 10 sec, 2.6 mm/s for 10 sec, 3.2 mm/s for 10 sec, 2.6 mm/s for 10 sec, and 2.0 mm/s for 10 sec.

Experiment	1	2	3	4	5	6	7	8	9
d (mm)	4.191	4.191	4.191	4.318	4.318	4.318	4.445	4.445	4.445
ω (rpm)	1600	1900	2100	1600	1900	2100	1600	1900	2100

Table 3: Constant Process Parameters for Group 3 Experiments. Rotation speed is 1600 rpm for 10 sec, 1900 rpm for 10 sec, 2100 rpm for 10 sec, 1900 rpm for 10 sec, and 1600 rpm for 10 sec.

Experiment	1	2	3	4	5	6	7	8	9
d (mm)	4.191	4.191	4.191	4.318	4.318	4.318	4.445	4.445	4.445
v (mm/s)	2.0	2.6	3.2	2.0	2.6	3.2	2.0	2.6	3.2

Table 4: Model Parameters for Axial Force Dynamic Model (Group 1).

Experiment	b	p_1	p_2	$-Kb/(p_1 \cdot p_2)$
1	−2.83	−17.8	−2.74	0.130
2	−1.16	−21.7	−1.72	0.1.29
3	−1.05	−59.9	−1.25	0.1.26
4	−2.88	−13.3	−4.09	0.131
5	−5.91	−7.00+4.86i	−7.00–4.86i	0.133
6	−2.90	−20.5	−3.36	0.135
7	−2.08	−16.2	−3.26	0.129
8	−3.47	−19.8	−3.74	0.125
9	−2.64	−34.5	−1.00	0.125
average	−2.25	−25.5	−2.65	0.129

Table 5: Relative Deviations of Process Variables for Different Experiments.

	F_x	F_y	F_z
ρ_{con}	$9.12 \cdot 10^{-2}$	$8.07 \cdot 10^{-2}$	$1.23 \cdot 10^{-2}$
ρ_{step}	$8.39 \cdot 10^{-2}$	$9.64 \cdot 10^{-2}$	$2.18 \cdot 10^{-2}$
ρ_{sin}	$9.82 \cdot 10^{-2}$	$9.22 \cdot 10^{-2}$	$4.19 \cdot 10^{-2}$
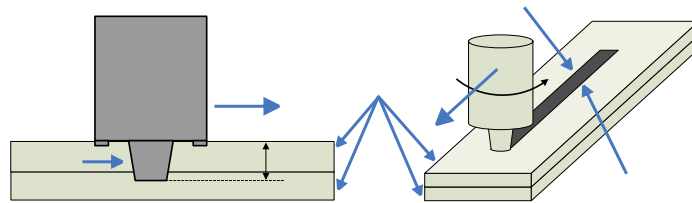
Figure 1: Friction Stir Welding Operation Schematics for Lap Welding.

Figure 2: IRB 940 Tricept Manipulator (left) and S4cPlus Controller (right).

Figure 3: FSW Head with Tool (left) and FSW Head Control Housing (right).
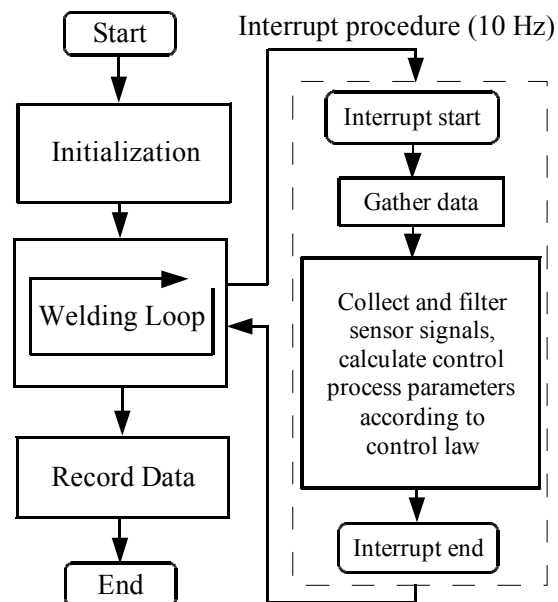
Figure 4: Robotic Friction Stir Welding Program Structure.
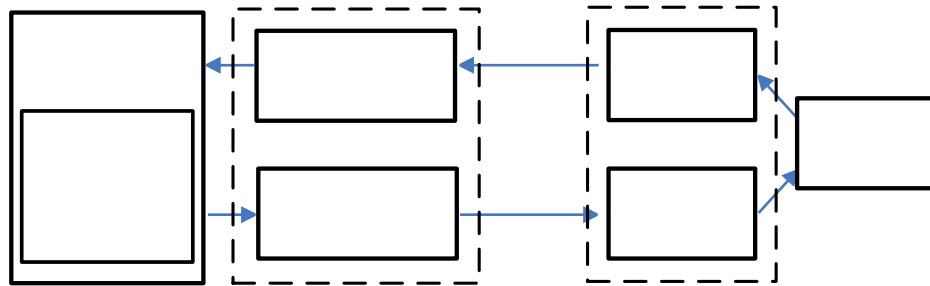
Figure 5: Robotic Friction Stir Welding Experimental System Structure.
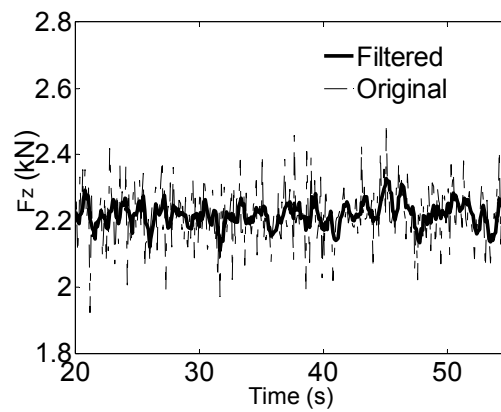
Figure 6: Comparison of Filtered and Original Measured Axial Force Signals during

Steady–State Portion of a FSW Operation. (v = 2.6 mm/s, ω = 1600 rpm, d = 4.191 mm).
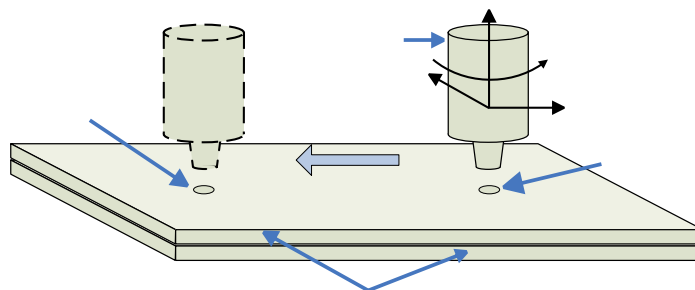
Figure 7: FSW Lap Joint Experimental Setup.

Figure 8: Nugget Cross Section with Slight Hooking Defect on Right Side. (ω = 1600 rpm, v = 2.6 mm/s, and d = 4.445 mm).
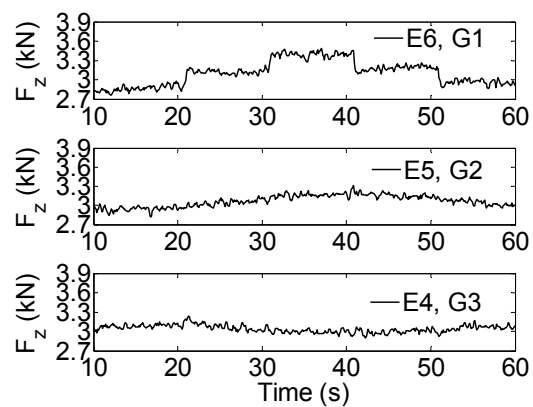
Figure 9: Axial Force Responses for Step Changes in Process Parameters. (E Corresponds to Experiment and G Corresponds to Group. Process Parameters Experience Step Changes at 20, 30, 40, and 50 sec).
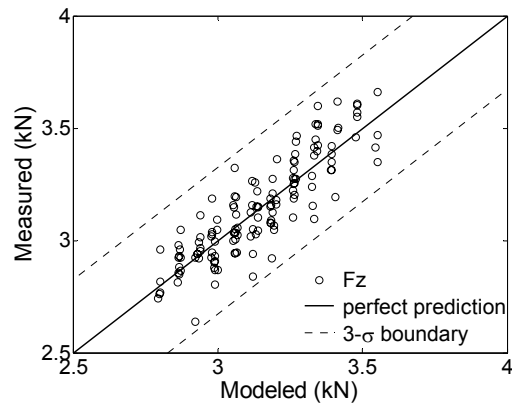
Figure 10: Modeled Versus Measured Steady–State Axial Force.
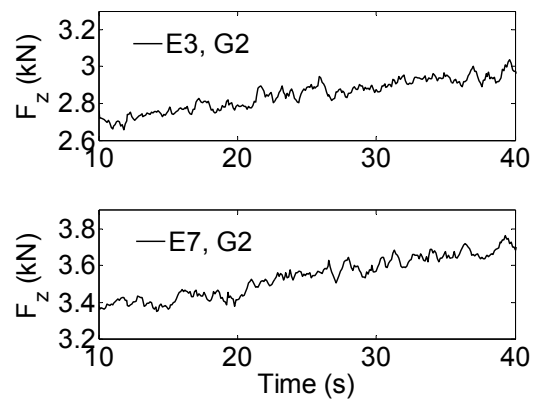
Figure 11: Axial Force Responses to Travel Speed Step Changes. (Travel Speed Step Changes Occur at 20 and 30 sec).
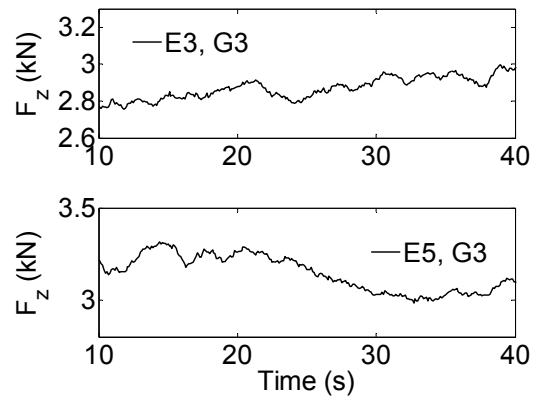
Figure 12: Axial Force Responses to Rotation Speed Step Changes. (Rotation Speed Step Changes Occur at 20 and 30 sec).
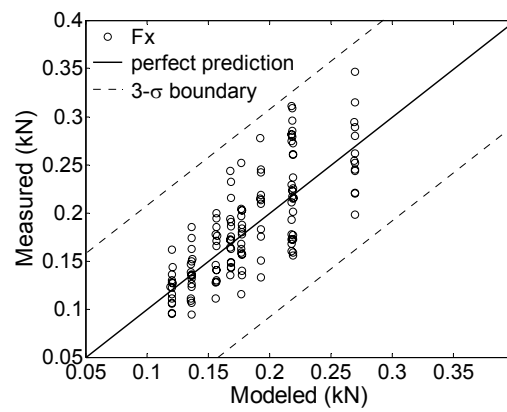
Figure 13: Modeled Versus Measured Steady–State Path Force.
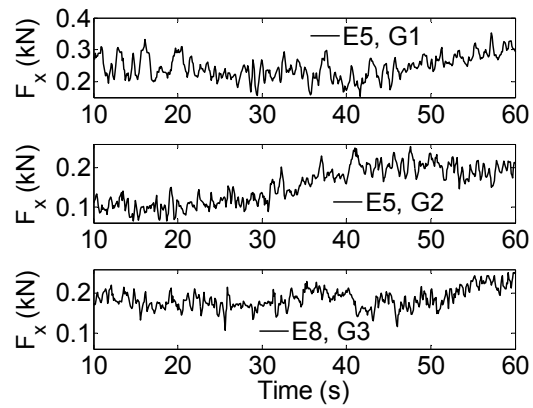
Figure 14: Path Force Transient Responses to Step Changes in Process Parameters. (Process Parameters Experience Step Changes at 20, 30, 40, and 50 sec).
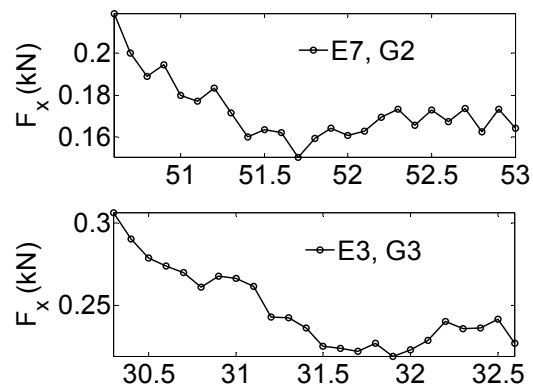
Figure 15: Path Force Transient Responses. (Top: Travel Speed Changed from 2.6 to 2.0 mm/s. Bottom: Rotation Speed Changed from 1900 to 2100 rpm).
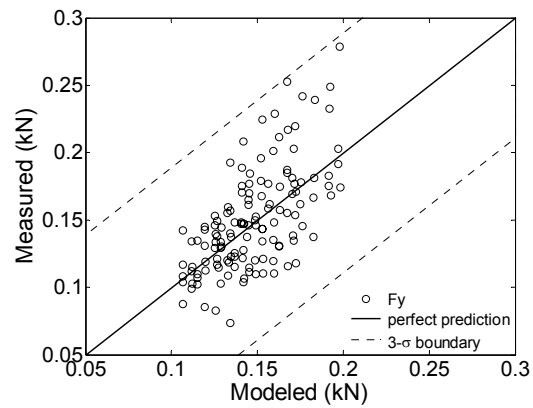
Figure 16: Modeled Versus Measured Steady–State Normal Force.
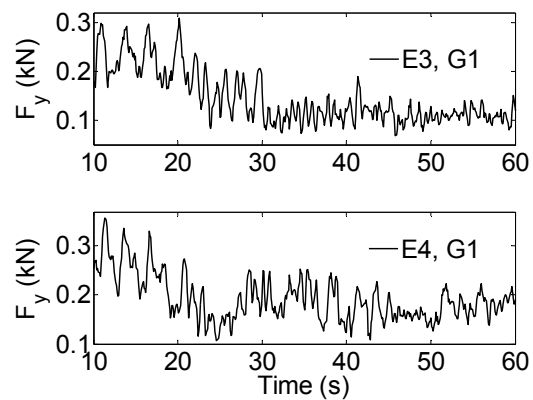
Figure 17: Normal Force Responses to Plunge Depth Step Changes. (Plunge Depth Step

Changes Occur at 20, 30, 40, and 50 sec).
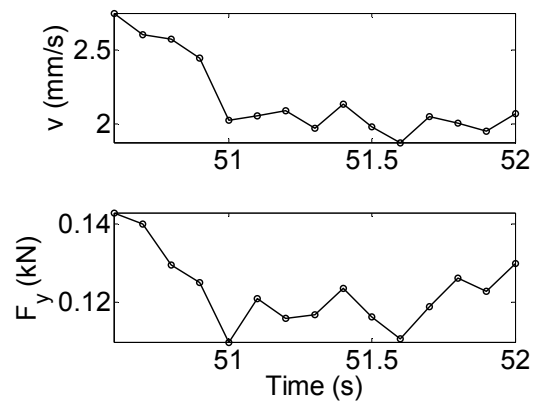
Figure 18: Normal Force Response to Travel Speed Step Change. (Experiment 9, Group 2).
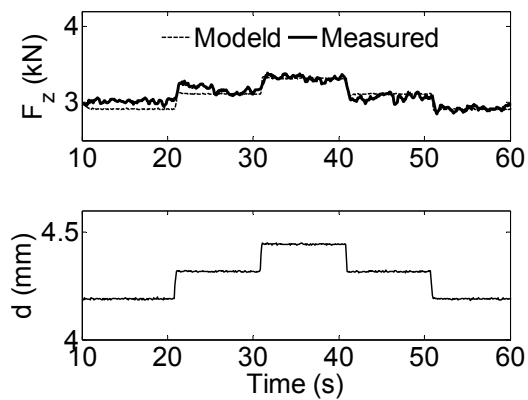
Figure 19: Measured and Modeled Axial Force for Step Changes in Plunge Depth.

(Experiment 1, Group 1, ω = 1600 rpm, v = 2.0 mm/s).
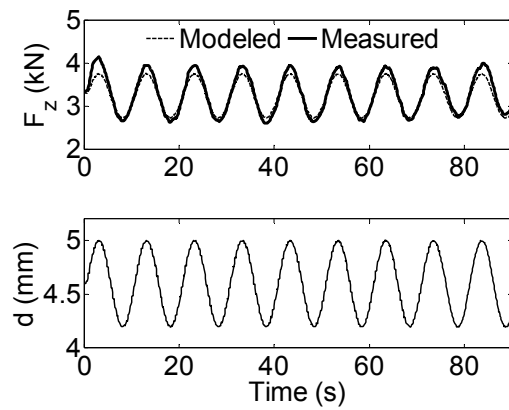
Figure 20: Measured and Modeled Axial Force for Sinusoidal Change in Plunge Depth.

(ω = 1600 rpm, v = 2.6 mm/s).
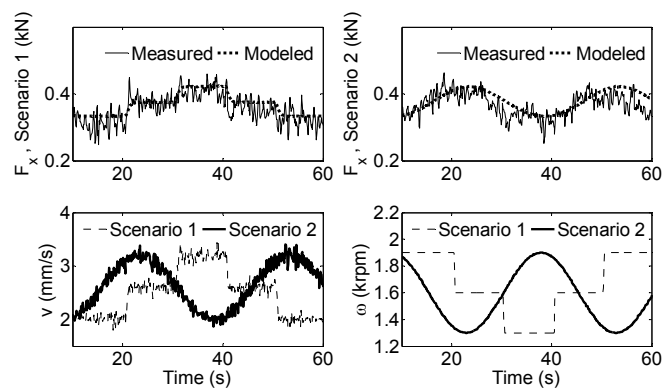
Figure 21: Path Force Model Validation Experimental Results. (d = 4.445 mm).
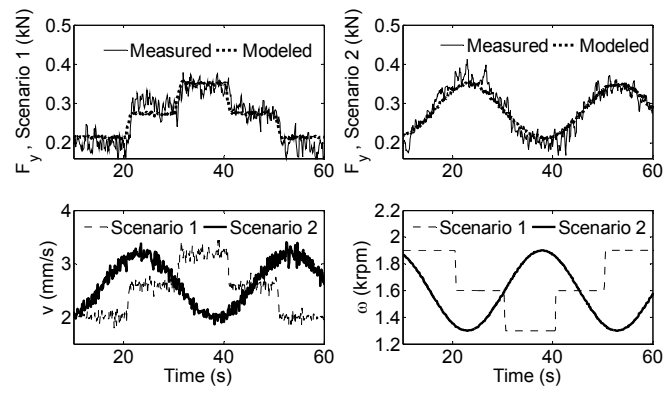
Figure 22: Normal Force Model Validation Experiments. (*d* = 4.445 mm).

II: Design and Implementation of Nonlinear Force Controllers for Friction Stir Welding Processes

Xin Zhao, Prabhanjana Kalya, Robert G. Landers, and K. Krishnamurthy

University of Missouri–Rolla, Mechanical and Aerospace Engineering Department,

1870 Miner Circle, Rolla, Missouri 65409–0050, USA

{xzvc8;pk34b;landersr;kkrishna}@umr.edu

Abstract

In Friction Stir Welding (FSW) processes, force control can be used to achieve good welding quality. This paper presents the systematic design and implementation of FSW force controllers. The axial and path forces are modeled as nonlinear functions of the FSW process parameters (i.e., plunge depth, tool traverse rate, and tool rotation speed). Based on the dynamic process and equipment models, nonlinear feedback controllers for the axial and path forces are designed using the Polynomial Pole Placement (PPP) technique. The controllers utilize a Smith–Predictor–Corrector (SPC) structure to compensate for the inherent equipment delay and the controller parameters are tuned to achieve the best closed loop response possible given equipment limitations. In the axial force controller implementation, a constant axial force is tracked, even when gaps are encountered during the welding process. In the path force controller implementation, surface and internal defects generation during the welding process is eliminated by regulating the path force.

Key words: Friction Stir Welding, Feedback Control, Polynomial Pole Placement, Smith–Predictor–Corrector

Nomenclature

d Plunge depth (*mm*)

d_c Commanded plunge depth (*mm*)

F_a Axial force (*kN*)

F_p Path force (*kN*)

f_d Frequency of plunge depth equipment model validation experiments (*Hz*)

f_s Sampling rate (*Hz*)

f_ω Frequency of tool rotation speed equipment model validation experiments(*Hz*)

G_m Gain margin (dB)

g Gap distance (*mm*)

P_m Phase margin (degree)

v Tool traverse rate (*mm/s*)

ω Tool rotation speed (*rpm*)

ω_c Commanded tool rotation speed (*rpm*)

1. Introduction

Friction Stir Welding (FSW) is a new solid state welding technology that has been used successfully in many joining applications. In FSW processes, a rotating non–consumable tool, consisting of a pin and shoulder, plunges into the part such that both the pin and shoulder are in contact with the part. The tool rotation induces gross material plastic

deformation due to an elevated temperature field. The tool travels along, or across, the intersection of two parts after dwelling for a specified amount of time, and joins the parts as the tool leaves the processing zone. This technique has advantages in that it can join materials that are difficult to weld by conventional welding processes, such as 2000 and 7000 series aluminum alloys, and part distortion and residual stresses after the process are low. The FSW process is also environmentally friendly because no harmful gases are generated during welding. Figure 1 shows the schematic of the FSW butt welding process.

Most current FSW processes are implemented on either a customized conventional machine or a programmable industrial robot [1]. For both platforms, one issue in FSW processes is that a control mechanism to maintain a constant axial force is necessary to achieve a quality weld due to improper fixturing, the existence of gaps between plates, and changes in plunge depth due to machine structural deformations. Smith [2] presented illustrations of robotic FSW with a serial industrial robot IRB 7600 working in the force feedback control mode. Strombeck [3] gave welding examples using the parallel industrial robot RIFTEC 600 with force feedback control. Cook [4] investigated the relationship between the step increment in plunge depth and the corresponding increment in the axial force and noted that a force controller stability problem could be caused by the transient response characteristic during the beginning welding stage. Most current axial force feedback control algorithms in FSW machines are proprietary and, to the author's knowledge, no systematic design techniques are available in the literature. In FSW processes the generation of surface and internal voids in the part is another considerable issue. These defects are generally caused by the improper

selection of process parameters. Experimental results revealed a relationship between the generation of these defects and the path force: when the path force is above a critical value, void defects are generated. This result suggests that a feedback path force controller can be designed to eliminate the generation of voids defects during FSW processes.

The rest of this paper is organized as follows. First, equipment utilized in this study and noise filtering are described. Dynamic FSW process models for the axial and path forces and the equipment dynamic models are presented. Then, the detailed design procedure of the force controllers using the Polynomial Pole Placement method implemented in a Smith–Predictor–Corrector structure is introduced. Lastly, experimental validations of the controllers are performed and discussed.

2. Experimental Equipment

The FSW system (Figure 2) used to conduct the experiments in this paper consists of a six degree of freedom robot (ABB IRB 940 Tricept robot), a FSW spindle head, a six axis force/moment sensor, and an open architecture control system. The robot has three non parallel telescopic translational joints and three rotational joints, and is retrofitted with a FSW spindle head to provide the rotational tool motion. The FSW spindle head (Figure 3) has a rotational axis driven by a 10 hp Exlar SLM115–368 servo motor with a rotational speed range of ±3000 rpm. The load capability of the spindle is 9 kN along the tool axis and 4.5 kN in the radial direction. The six–axis force/moment sensor system (JR3 Inc. model 75E20S–M125A–A 6000N1150) provides the measurements of the

process loading: the forces in three orthogonal directions and moments about each direction. The output analog voltage signal ranges are ±10.0 *V*. The rated sensor forces are 6 *kN* in the x and y–directions and 12 *kN* in the z–direction. The rated moments are 1,150 *N·m* about all three directions. The teach pendant is used to manually control and program the robot.

The IRB 940 Tricept robot uses an S4cPlus robot control unit with RAPID as the programming language. RAPID is a high level language which enables the operator to pre–program the processing sequence and control algorithm in simple text formats, upload the source programs to the control unit, and then compile and execute the code. Figure 4 illustrates the basic structure and functional blocks of the program used for the experiments conducted in this paper. The program consists of the initialization routines executed at the beginning, a main welding loop executing in real–time during the welding process, and the, and the data storage routines executed at the end. An interrupt procedure with an interval of 0.1 *sec* is triggered to provide a constant frequency of data acquisition and process parameter outputs as soon as the main welding loop is entered. During the interrupt procedure, the sensor data (i.e., forces, moments, and measured process parameters) are collected and the output signals (i.e., commanded process parameters) are calculated. These output signals are sent to their perspective amplifiers during the main welding loop and, after the main loop finishes, all collected sensor data are saved to the control unit hard disk.

The experimental data contains significant electrical noise. Therefore, a five–point moving average was empirically determined to provide good data filtering without

significant signal delay and unduely taxing the system's limited computational bandwidth. The filtered force signal is

$$Y_f(i) = \frac{1}{5}\left(Y_m(i) + Y_m(i-1) + Y_m(i-2) + Y_m(i-3) + Y_m(i-4)\right) \tag{1}$$

where $Y_f(i)$ is the filtered force at the ith iteration and $Y_m(i)$ is the measured force at the ith iteration. After implementing the filter, the standard deviation of the steady state force data with constant process parameters decreases from 0.062 kN to 0.031 kN.

3. Process Modeling

In this paper, the controller designs are based on empirical dynamic models of the FSW process of 6061–T6 aluminum alloy (detailed composition by weight: Al: 97.9%, Si: 0.60%, Cu: 0.30%, Mg: 1.0%, and Cr: 0.20%). Based on the work of Zhao *et al*. [5], the axial (F_a) and path (F_p) forces are developed using the Least Square and Recursive Least Square techniques and can be modeled as second and first order systems, respectively, with the plunge depth and tool rotation speed, respectively, as the input process parameters. Other factors can be treated as disturbances (e.g., fixturing) or are constant during the operation (e.g., material properties, tool geometry, travel and work angle). Given a sampling frequency of 10 H_z, those models are converted into the discrete time domain with a Zero–Order–Hold and, respectively, are

$$F_a(z) = \frac{v^{0.0970}\omega^{-0.230}\left(0.136z - 0.108\right)}{z^2 - 0.846z + 5.99\cdot10^{-2}}d^{2.207}(z) \tag{2}$$

$$F_p(z) = \frac{2.20\cdot10^{-2}v^{0.999}}{z - 0.854}\omega^{-1.23}(z) \tag{3}$$

4. Equipment Dynamic Modeling

Two process parameters (i.e., plunge depth and tool rotation speed) will be adjusted during the welding process to regulate the welding forces. Due to the dynamic characteristics of the actuators and the communication delays that exist between the processors handling the high and low level computations, these parameters cannot change immediately after a process parameter modification command is issued. Instead, a dynamic relationship exists between the commanded and measured process parameters. According to the nonlinear relationship between the axial and path forces and the process parameters, i.e., d and ω, as shown in equations (2) and (3), modeling the dynamic relationships between $d^{2.21}$ and $d_c^{2.21}$, and $\omega^{-1.23}$ and $\omega_c^{-1.23}$ is more convenient in that the axial and path force models and the models from the commanded to measured parameters can be easily combined together to build overall models between the commanded parameters and the forces. Step change experiments for these parameters were conducted to determine these relationships. Experimental results show that the relationships between the commanded and measured parameters can be described by a pure delay and a first order transient response. Figures 5 and 6 show experimental results for the tool rotation speed and plunge depth, respectively, for step changes in the commanded process parameters. The numbers of delay periods are visually observed and the time constants of the transient responses are estimated by the Least Square method using the commanded and measured data. For each parameter, nine runs are conducted and therefore, 36 transient response data sets are collected, as shown in Figures 7 and 8.

Taking the averages of the delay time and time constant, the dynamic relationships between the commanded and measured plunge depth and tool rotation speed, respectively, are

$$\frac{d^{2.21}(s)}{d_c^{2.21}(s)} = \frac{e^{-0.531s}}{0.151s+1} \qquad (4)$$

$$\frac{\omega^{-1.23}(s)}{\omega_c^{-1.23}(s)} = \frac{e^{-0.294s}}{0.114s+1} \qquad (5)$$

where ω and d are the tool rotation speed and plunge depth, respectively, and ω_c and d_c are the commanded tool rotation speed and plunge depth, respectively. The standard deviations of the plunge depth and rotation speed delay times, and the plunge depth and tool rotation speed response time constants, are $4.67 \cdot 10^{-2}$ sec, $6.30 \cdot 10^{-2}$ sec, $5.70 \cdot 10^{-2}$ sec, and $5.59 \cdot 10^{-2}$ sec, respectively. The smaller standard deviations of the plunge depth delay time and time constant indicate that it has a more consistent response dynamics compared to the tool rotation speed. Also, the results show that the tool rotation speed has a relatively smaller delay time compared to the plunge depth, indicating a fast response between the measured and commanded parameter. This is due to the fact that the spindle rotation and the linear motion are implemented on two different computational and control system, as mentioned in the experimental equipment chapter. Since the welding program operates at a sampling frequency of $f_s = 10$ H_z, the number of delayed periods can be calculated based on the average delay time T and f_s as $N = round(T / f_s)$.

The equipment models relating the measured and commanded process parameters in the discrete domain, using a Zero–Order–Hold transformation, are

$$\frac{d^{2.21}(z)}{d_c^{2.21}(z)} = \frac{0.484}{z - 0.516} z^{-5} \qquad (6)$$

and

$$\frac{\omega^{-1.23}(z)}{\omega_c^{-1.23}(z)} = \frac{0.587}{z - 0.413} z^{-3}$$ (7)

A series of sinusoidal experiments were conducted to validate the plunge depth and tool rotational speed equipment models. The commanded plunge depth and tool rotation speed are $d_c = 4.318 + 0.127\sin(2\pi f_d t)$ and $\omega_c = 1900 + 300\sin(2\pi f_\omega t)$, respectively. The frequencies of the sinusoidal experiments are limited by the rate limits imposed on both plunge depth and tool rotation speed, which are 0.2 *mm/s* and 1000 *rpm/s*, respectively. Therefore, the maximum frequencies for the plunge depth and tool rotation speed sinusoidal experiments, are 0.251 H_z and 0.531 H_z, respectively. Four frequencies for each parameter are selected within these ranges. The model Bode diagrams and the measured magnitude ratio (*M*) and phase shifts (ϕ) are shown in Figures 9 and 10.

The Bode Diagrams indicate that the validation experimental results fit the models very well. The maximum differences between the modeled and measured magnitudes and phase shifts of plunge depth are 0.145 dB and −8.70°, respectively; and the maximum differences between the modeled and measured magnitudes and phase shifts of tool rotation speed are 0.403 dB and 12.0°, respectively. However, the modeled and measured results show slight differences in high frequency range for both equipment models. One explanation to this phenomenon is that in the discrete time models, the model delay time is rounded to integers based on the sampling rate, which is either

smaller (for the plunge depth equipment model) or larger (for the tool rotation speed equipment model) compared to the actual delay time.

5. Controller Design

In this section, feedback controllers utilizing the Polynomial Pole Placement technique are designed to regulate the axial and path forces at constant values. The controllers are both implemented in a Smith–Predictor–Corrector (SPC) structure to compensate for the inherent equipment delay. The two controllers have the same closed loop system block diagram, as shown in Figure 11. The parameter F_r is the reference force, F is the measured force, E is the error between the reference and measured forces, U is the control signal, C is the controller transfer function, G is model force process transfer function, and n is the number of equipment delay periods.

Since the sampling and control signal generating rate is limited to $f_s = 10\ H_z$, the operating bandwidth is 0–5H_z. The design procedure consists of following steps:

1. Calculate the process model $G(z)$'s zeros and poles.

2. Choose the poles of the closed loop system based on the results of Step 1.

3. Calculate the controller transfer function $C(z)$ using the Polynomial Pole Placement method with the Internal Model Principle based on the closed loop poles chosen in Step 2.

4. Evaluate the closed loop system's stability and robustness within the operating bandwidth using stability margins and the sensitivity function.

The above design procedure is iterative, and Steps 2–4 may need to be repeated according to the stability and robustness evaluation results and the experimental

validation results. Detailed design steps are discussed in the following sections for the axial and path force controller designs.

5.1 Axial Force Controller

The plant dynamic model $G_0(z)$ is a combination of the axial force process model and the equipment dynamic model, as presented in equations (2) and (6), and is

$$G_0(z) = G(z) z^{-5} \qquad (8)$$

where

$$G(z) = \frac{b(z)}{a(z)} = \frac{v^{0.0970} \omega^{-0.230} (0.0621z - 0.0497)}{z^3 - 1.42z^2 + 0.566z + 0.0518} \qquad (9)$$

In the initial design step of the controller transfer function $C(z)$, the inherent equipment delay is ignored and

$$C(z) = \frac{p(z)}{q(z)} \qquad (10)$$

The closed loop transfer function is

$$\frac{F(z)}{F_r(z)} = \frac{p(z)b(z)}{q(z)a(z) + p(z)b(z)} \qquad (11)$$

The desired closed loop characteristic polynomial is $\alpha(z)$; therefore, the following equation must be hold

$$q(z)a(z) + p(z)b(z) = \alpha(z) \qquad (12)$$

Given the system plant transfer function, as shown in equation (9), and a specified closed loop characteristic polynomial, the coefficients of $p(z)$ and $q(z)$ can be determined by equating like coefficients in equation (12).

As shown in equation (9), $G(z)$ has one zero located at 0.08012 and three poles located at 0.516, 0.772, and 0.130. These poles correspond to three poles: –6.62, –2.59, and –20.4, after being mapped from the z–plane to the s–plane using $s = \ln(z) \cdot f_s$, where f_s is the sampling frequency. The first pole corresponds to the time constant of 0.151 *sec* due to the equipment first order response, and the second and third poles correspond to two first order responses with time constants of 0.387 and 0.0490 *sec*, respectively, due to the axial force process dynamic.

The closed loop characteristic polynomial $\alpha(z)$ is 6th order. The initial choice for this polynomial is

$$\alpha(z) = (z - r_1)(z - r_2) R(z) \tag{13}$$

where r_1 and r_2 are two dominant poles, and $R(z)$ is a 4th order polynomial. Considering that the plant transfer function $G(z)$ has three poles with different time constants, the polynomial $R(z)$ is manipulated to contain two poles at the origin and two poles that are identical to the two poles of $G(z)$ with the smallest time constants. Therefore,

$$R(z) = z^2 (z - 0.5157)(z - 0.1301) \tag{14}$$

Substituting equations (13) and (14) into equation (12) yields

$$\begin{aligned} p(z)b(z) = {} & z^2 (z - r_1)(z - r_2)(z - 0.5157)(z - 0.1301) \\ & -q(z)(z - 0.7722)(z - 0.5157)(z - 0.1301) \end{aligned} \tag{15}$$

Substituting equation (15) into equation (11) and canceling the same polynomial factors yields

$$\frac{F(z)}{F_r(z)} = \frac{z^2 (z - r_1)(z - r_2) - q(z)(z - 0.7722)}{z^2 (z - r_1)(z - r_2)} \tag{16}$$

Equation (16) shows that by manipulating the pole locations of $\alpha(z)$, the order of the closed loop characteristic polynomial is reduced from 6 to 4. Another pole placement strategy is that $\alpha(z)$ contains one dominant pole and $R(z)$ contains three poles of the plant transfer function $G(z)$. However, the system evaluation performed in the next section showed that the closed loop system based on this pole placement has poor stability and robustness against the modeling error, and therefore is abandoned. Generally the rise time of the closed loop system should have at least 4–10 sampling periods to maintain the system stability [6]. Since the sampling period is 0.1 *sec*, r_1 and r_2, the dominant poles of $\alpha(z)$, are initially chosen as 0.936 and 0.819, which correspond to time constants of 1.5 *sec* and 0.5 *sec*, respectively. The parameter r_1 is tuned experimentally by decreasing its value, without inducing instability and r_2 is tuned to the value that minimizes the sensitivity of the closed loop system, as discussed in the following section. The final design values of r_1 and r_2, are 0.9131 and 0.7386, which correspond to time constants of 1.1 *sec* and 0.33 *sec*, respectively. Substituting r_1, r_2 and equation (14) into (13), the closed loop characteristic polynomial is

$$\alpha(z) = z^6 - 2.298z^5 + 1.808z^4 - 0.5463z^3 + 0.04525z^2 \tag{17}$$

For the experiments conducted in this paper, the reference force is constant; therefore, the denominator of the controller transfer function must contain a factor of $(z–1)$. By denoting $q(z) = q_2(z)(z–1)$ to ensure the controller has integral action to track constant references, equation (12) is transformed into

$$\begin{aligned}
&q_2(z)(z-1)\left(z^3 - 1.424z^2 + 0.5662z + 0.05184\right) \\
&+ p(z)(0.0621z - 0.0497)v^{0.0970}\omega^{-0.230} \\
&= z^6 - 2.298z^5 + 1.808z^4 - 0.5463z^3 + 0.04525z^2
\end{aligned} \tag{18}$$

Given that the system order is 3, for a proper controller to exist such that equation (18) is satisfied, the orders of $p(z)$ and $q_2(z)$ are, respectively, 3 and 2. Controller coefficients are calculated by equating like coefficients of equation (18), and the controller transfer function is

$$C(z) = \frac{p(z)}{q(z)} = \frac{\left(1.175z^3 - 9.328 \cdot 10^{-2} z^2 - 0.3511z + 4.467 \cdot 10^{-2}\right) v^{-0.0970} \omega^{0.230}}{z^3 - 0.8795z^2 - 7.768 \cdot 10^{-2} z - 4.286 \cdot 10^{-2}} \quad (19)$$

It is noted that the numerator contains power terms of v and ω, and therefore, the controller is able to compensate for the variations in the traverse rate and the tool rotation speed.

Since the plant model contains modeling inaccuracies, the sensitivity function and the stability margins are checked during the design procedure to ensure the closed loop system has sufficient stability and robustness. For the closed loop system not implemented in the SPC structure, the sensitivity function is

$$S(z) = \frac{1}{1 + C(z)G(z)} \quad (20)$$

The sensitivity function can be interpreted as the ratio of the change in the closed loop transfer function to the change in the open loop transfer function, [7]

$$\frac{d(H_{cl})}{H_{cl}} = S \frac{d(H)}{H} \quad (21)$$

where $H(z) = C(z)G(z)$ is the open loop transfer function and $H_{cl}(z) = H(z)(1 + H(z))^{-1}$ is the closed loop transfer function. The sensitivity function $S(z)$ is used as a measure of the closed loop system sensitivity to noise, external disturbances, and modeling errors.

Substituting $z = e^{i\omega T}$, where T is the sampling period, i is the imaginary number, and ω is frequency, into equation (20) yields

$$S\left(e^{i\omega T}\right) = \frac{1}{1 + C\left(e^{i\omega T}\right)G\left(e^{i\omega T}\right)} \tag{22}$$

The inverse of $\left|S\left(e^{i\omega T}\right)\right|$ is $\left|1 + C\left(e^{i\omega T}\right)G\left(e^{i\omega T}\right)\right|$, which represents the distance from a point of the Nyquist curve of the open loop transfer function $C\left(e^{i\omega T}\right)G\left(e^{i\omega T}\right)$ to the critical point -1. To have a reasonable robustness and maintain stability against modeling errors, $\left|S\left(e^{i\omega T}\right)\right| < 2$.[6] The value of $\left|S\left(e^{i\omega T}\right)\right|$ with the system operating bandwidth of $0 < \omega < 5H_z$ is plotted in Figure 12. The result indicates that the desired closed loop system meets the sensitivity requirement.

The stability margins consist, respectively, of the gain margin G_m and phase margin P_m

$$G_m = -20\log_{10}\left|H\left(i\omega_1\right)\right| \tag{23}$$

$$P_m = \angle H\left(i\omega_2\right) \tag{24}$$

where ω_1 is the phase crossover frequency where the phase is $-180°$ and ω_2 is the magnitude crossover frequency where the magnitude of H is 1. The closed loop system is stable only if both G_m and P_m are positive. Generally, G_m should be greater than 6 dB, and P_m should be greater than $30°$ so that the closed loop system has sufficient robustness against the modeling errors.[8] Figure 13 shows the Bode Diagram with the marked magnitude and phase margins, which both meet the stability margin requirements.

The next step of the controller design is to implement the controller in a Smith–Predictor–Corrector (SPC) structure. The overall closed loop system diagram is shown in Figure 11 where $n = 5$ is the number of the equipment delay periods. The modified control law is

$$
\begin{aligned}
u(k) = {} & 0.879u(k-1) + 7.77 \cdot 10^{-2} u(k-2) + 4.29 \cdot 10^{-2} u(k-3) \\
& + 1.18 v^{-0.0970} \omega^{0.230} \left[e(k) - e_1(k) \right] \\
& - 9.33 \cdot 10^{-2} v^{-0.0970} \omega^{0.230} \left[e(k-1) - e_1(k-1) \right] \\
& - 0.351 v^{-0.0970} \omega^{0.230} \left[e(k-2) - e_1(k-2) \right] \\
& + 4.47 \cdot 10^{-2} v^{-0.0970} \omega^{0.230} \left[e(k-3) - e_1(k-3) \right]
\end{aligned}
\tag{25}
$$

where

$$
\begin{aligned}
e_1(k) = {} & 1.42 e_1(k-1) - 0.566 e_1(k-2) + 5.18 \cdot 10^{-2} e_1(k-3) \\
& + 6.21 \cdot 10^{-2} v^{0.0970} \omega^{-0.230} \left[u(k-2) - u(k-7) \right] \\
& - 4.97 \cdot 10^{-2} v^{0.0970} \omega^{-0.230} \left[u(k-3) - u(k-8) \right]
\end{aligned}
\tag{26}
$$

and $u(k) = d_c^{\alpha}(k)$, is the control signal for the plant transfer function. The commanded plunge depth is determined using the nonlinear mapping $d_c(k) = u^{-\alpha}(k)$. Due to the load capacity of the FSW robot and the possibility of tool breakage, control signal saturation is required for both the plunge depth and the rate of change of the plunge depth. First, the tool geometry restricts the range of the plunge depth: the tool shoulder must maintain contact with the plate's surface and a plunge depth that is too deep generates excessive material flow away from the welding surface and reduces the thickness of the welded part. Since the pin length is 4.165 *mm*, the plunge depth is chosen to be in the range of 4.17 to 4.60 *mm*. Also, a rate limit of 0.20 *mm/s* is applied based upon operator's experience. Magnitude and rate signal saturations are implemented within the controller program.

5.2 Path Force Controller

The path force controller is also designed using the Polynomial Pole Placement technique with the application of the Internal Model Principle. The plant transfer function $G_0(z)$, incorporating the path force process model and the equipment rotational speed model, is

$$G_0(z) = G(z) z^{-3} \tag{27}$$

where

$$G(z) = \frac{b(z)}{a(z)} = \frac{1.29 \cdot 10^{-2} v^{0.999}}{z^2 - 1.27z + 0.353} \tag{28}$$

where $r_1 = 0.854$ and $r_2 = 0.413$. The first pole is due to the path force process model dynamics and the second pole is due the equipment model dynamics. The operating bandwidth is again $\omega = 5\ H_z$.

The order of the path force dynamic model is 2; therefore, the order of the closed loop characteristic polynomial is 4. Similar to the axial force controller design, the closed loop characteristic polynomial $\alpha(z)$ is manipulated to contain the factors of $a(z)$, so that the order of the closed loop transfer function can be reduced. An initial design of $\alpha(z)$ is

$$\alpha(z) = (z - r_0)(z - r_1)(z - r_2) z \tag{29}$$

where r_0 is the dominant pole and r_1 and r_2 are identical to the plant transfer function poles. The time constant of the dominant pole is assigned as 1.2 *sec*, based on the experimental results, so that closed loop system response is fast and the system still has sufficient stability and robustness against the noise and modeling errors. Therefore, $r_0 = 0.9260$. Substituting r_0, r_1, and r_2 into equation (29) yields

$$\alpha(z) = z^4 - 2.187z^3 + 1.518z^2 - 0.3244z \tag{30}$$

The controller transfer function is

$$C(z) = \frac{p(z)}{q(z)} = \frac{\left(6.188z^2 - 7.841z + 2.182\right)v^{-0.999}}{z^2 - 0.9200z - 7.996 \cdot 10^{-2}} \tag{31}$$

The closed loop design is also evaluated by computing the sensitivity function and stability margins. Figure 14 shows the value of sensitivity function in the range of $0 < \omega < 5$ H_z, and the maximum value is 1.10. Figure 15 shows the Bode Diagram with the marked stability margins. The magnitude and phase margins are 22.6 dB and 83.9°, respectively. Therefore, the requirements for both the sensitivity function and stability margins are satisfied.

Similar to the axial force controller design, the path force controller is implemented in a Smith–Predictor–Corrector structure and the control law is

$$u(k) = 0.920u(k-1) + 8.00 \cdot 10^{-2}u(k-2) + 6.19v^{-0.999}\left[e(k) - e_1(k)\right]$$
$$-7.84v^{-0.999}\left[e(k-1) - e_1(k-1)\right] + 2.18v^{-0.999}\left[e(k-2) - e_1(k-2)\right] \tag{32}$$

where

$$e_1(k) = 1.27e_1(k-1) - 0.355e_1(k-2) + 1.29v^{0.999}\left[u(k-2) - u(k-5)\right] \tag{33}$$

and $u(k) = \omega_c^\gamma(k)$, is the control signal for the plant transfer function. The commanded plunge depth is determined using the nonlinear mapping $\omega_c(k) = u^{-\gamma}(k)$.

6. Experimental Validation

In this section, lap welding experiments are conducted to validate the performances of the axial and path force controllers. Figure 16 shows the lap welding experimental setup. For the axial force controller, three scenarios are conducted: five experiments to track step–

wise axial reference forces with different combinations of tool traverse rate and tool rotational speed, six experiments to track a constant axial reference force while welding across skin–to–skin and substructure gaps with different combinations of tool traverse rate and tool rotational speed, and four experiments to track constant axial reference forces while welding along gaps of different sizes. For the path force controller, three scenarios with a constant plunge depth are conducted: three experiments to track step–wise reference path forces with different tool traverse rates, four experiments to track step–wise reference path forces while welding along gaps of different sizes, and experiments to eliminate worm–hole generation by tracking a constant traverse reference force.

6.1 Axial Force

In the first set of axial force controller validation experiments, the tool traverse rate and tool rotation speed are constant and the reference axial force is changed twice in a step–wise manner. The reference force is F_{r1} for the first third of the welding distance, F_{r2} for the second third, and F_{r3} for the last third. Five experimental runs with different combinations of tool traverse rate and tool rotation speed are conducted to validate the controller's performance. Given the specific tool traverse rate, tool rotation speed, and the pre–selected plunge depth range, the reference force values are assigned within the calculated axial force range based on the axial force model, and then adjusted according to experimental results, so that the tool shoulder maintains a proper contact with the plate surface and good weld quality is obtained (i.e., neither voids defects nor excessive flash

are generated). Table 1 shows the process parameter combinations and reference axial forces for the five experimental runs.

Figures 17–21 show the experimental results of the axial force controller validation experiments with step–wise reference forces. The plots show the measured axial forces tracked the reference forces well, even when extreme process parameter values were applied. Table 2 gives the averages and standard deviations of the axial forces during the three steady–state portions of each run. The standard deviations are bellow 1% of the averages' magnitudes, except for the second steady–state of run #4, where the large tracking error is caused by an sudden external disturbance, which could be caused by the lack of plate surface flatness, the material defects, or the electrical noise. It is also observed that during the steady–states where the axial forces are constant, the plunge depth has significant variations. Two reasons may contribute to this phenomenon: 1) the fixturing force is not uniform, which causes that the plate surface is not a perfect plane; 2) due to the size limit of the plate, thermal boundary conditions vary significantly during the weld, especially when the tool starts from one end of the plate and approaches the other end, which causes the axial force changes and therefore, causes the plunge depth changes.

The next set of experiments explored the effects that skin–to–skin and substructure gaps have on the axial force controller. A four–piece experimental setup, illustrated in Figure 22, is utilized for these experiments. Two plates, separated by shims of constant thickness, are placed on the top, forming a skin–to–skin gap. Two plates, also separated by shims with the same thickness, are placed on the bottom, forming a substructure gap. The welding start and end locations are selected such that the welding

path goes across both gaps. Two groups of experiments are conducted to illustrate the effect of the force controller: experiments 1–6 utilize constant force control for different combinations of v and ω and experiments 7–12 utilize a constant plunge depth for the same combinations of v and ω. The reference axial force for each run in the first group was selected, based on experience, such that the tool shoulder maintained full contact with the plate surface and excessive flash and voids defects were not generated. The plunge depth for each run in the second group was selected based on the axial force model to maintain the reference force in the first group, given the combinations of v and ω. Figures 23–28 show the comparisons between the experimental results for both groups, with the same combinations of v and ω. In these figures, sub–plots 1 and 2 show the force control results, and sub–plot 3 shows the corresponding constant plunge depth results. On each sub–plot, the three dotted lines on the left portion of the figure indicate the times when the sides and center of the tool shoulder encounters the substructure gap, and the three dotted lines on the right indicate the times when the sides and center of the tool shoulder encounters the skin–to–skin gap. It is observed that when the force controller is implemented, a constant axial force is maintained at the reference value during the welding process even when skin–to–skin and substructure gaps were encountered. When the plunge depth was constant, the axial force dropped significantly when crossing both the skin–to–skin and substructure gaps with the gap sizes greater than zero. This is due to the fact that as the tool encounters less material and thus, less axial force is applied to the tool. Another observation is that and the axial force is not significantly affected by the gaps with zero size.

The average axial forces and the standard deviations for these two groups of experiments are shown in Table 3. It is observed that for runs with lower tool traverse rate, the difference between the axial force standard deviations of experiments with constant force control and experiments with constant depth is larger as compared to those with higher tool traverse rate. One explanation is that when the tool traverse rate is lower, the time period for the tool to travel crossing the gap is longer, which causes more axial force decrease, and therefore the improvement by implementing the controller is relatively significant. The constant force control has much better performance as compared to the constant plunge depth control. It is observed that the measured axial force tends to vary from the reference force with the constant plunge depth, which might be a result of many causes including the substructure and skin–to–skin gaps, the material inhomogeneity, thermal condition variations, and axial force modeling error.

The third set of axial force validation experiments is designed to test the controller's performance in welding along a skin–to–skin gap. The experimental setup is similar to the four–piece experiments, except that the gap in the top plate is along the weld direction and there is no gap in the bottom plate. Four configurations of gap size are applied: a constant gap of 0.381 *mm*, a constant gap of 0.762 *mm*, a tapered gap increasing linearly from 0.381 to 0.762 *mm* and a constant gap of 0 *mm* along the weld path. The process parameters are identical to run #3 in Table 1, where the controller has the best performance and the reference axial force is 3.00 *kN*. Figures 29–32 show the experimental results, and Table 4 gives the averages and standard deviations of the axial forces during three steady–state portions of each run. The results show that the axial force

controller also works well in welding along a gap, and the axial force is not significantly affected by the existence of gaps within the pre–selected size range.

6.2 Path Force

In the first set of path force controller validation experiments, the controller is implemented to regulate the path force to track constant reference forces and the plunge depth and tool traverse rate are constant. According to the path force model, the plunge depth does not affect the force significantly; therefore, a plunge depth of 4.20 *mm* is selected to ensure that the tool shoulder maintains contact with the material surface and that excessive flash is not generated during the weld. Three experiments were conducted with different traverse rates. The reference force levels for each experiment are selected based on the path force dynamic model to maintain the tool rotation speed within the pre– selected range (1600–2100 *rpm*) and the reference force changes from the highest (F_{r1}) to the lowest (F_{r2}) in a step–wise manner in the middle of the weld. Figures 33–35 show the experimental results and Table 5 shows the process parameters and the averages and standard deviations of the path force during two steady–states for each experiment. The results show the path force tracks the reference force well. However, compared to the axial force controller experiments, the path force experiments have relatively more variation. At least two factors contribute to this phenomenon: 1) the path force has a much lower magnitude (0.1–0.4 *kN*) than the axial force (2.5–3.5 *kN*); therefore, the signal to noise ratio is less and 2) the path force dynamic model is less accurate compared to the axial force model.[5]

The second set of path force validation experiments is designed to examine the controller's performance in welding along a skin–to–skin gap. The experimental setup is shown in Figure 36. Four gap sizes are examined: a constant gap of 0.381 *mm*, a constant gap of 0.762 *mm*, a tapered gap increasing linearly from 0.381 to 0.762 *mm*, and a constant gap of 0 *mm* along the weld path. The reference force takes a step–wise change from F_{r1} to F_{r2} in the middle of the weld. A constant traverse rate of 3.2 *mm/s*, under which the path force has the smallest standard deviation in tracking the lower force, is applied for all four experiments. Due to the presence of the gap, a constant plunge depth of 4.25 *mm*, 0.05 *mm* deeper as compared to the experiments without gaps, is applied to achieve the same path force level. Figures 37–40 show the experimental results and Table 6 shows the tracking performance. The results show that the controller also works well in welding along a skin–to–skin gap and the path force is not significantly affected by the presence and the size of a gap.

The third set of experiments is designed to demonstrate the ability of the path force controller to eliminate the generation of voids defects during the welding process. In the experiment, the plunge depth is 4.20 *mm* to ensure the shoulder maintains contact with the material surface and the tool traverse rate is 3.20 *mm/s*, so that a good tracking precision is achieved, The initial tool rotation speed is 800 *rpm*. During the first 20 seconds, the controller is not implemented and after 20 seconds, the controller is turned on to regulate the path force at the reference value of 0.22 *kN*. The reference force value was selected so that a good weld surface was observed without voids defects or the generation of excessive flash. The experimental results are shown in Figure 41. It is observed that the implementation of the controller maintained the path force at a constant

value. In the steady–state of weld with force control (26.5–48.0 *sec*), the average value of path force is 0.215 *kN* and the standard deviation is $0.795 \cdot 10^{-2}$ *kN*. Figure 42 shows nugget cross–section pictures of the weld during the steady–states both with force control (5.0–20.0 *sec*) and with constant tool rotation speed (20.0–48.0 *sec*). It is observed that with the implementation of the path force controller, voids defects, as shown in sub–plot (b), are eliminated, as shown in sub–plot (a).

7. Summary and Conclusions

Model–based, nonlinear axial and path force controllers were designed using the Polynomial Pole Placement technique with the Internal Model Principle. The equipment dynamics between the commanded and measured process parameters were also modeled to build the models from the commanded parameters to the process variables The controllers were implemented in a Smith–Predictor–Corrector structure to compensate for the inherent equipment delay. Detailed design procedures were introduced and several experiments were conducted to validate both the equipment models and controllers' performance.

The axial force controller works well in tracking constant forces despite the presence of gaps both along and across the weld path. The path force controller is also able to track constant forces with the presence of a gap along the weld path, although the tracking precision is relatively lower compared to the axial force controller due to the smaller signal to noise ratio and the modeling inaccuracies in the path force model. One validation experimental scenario showed that the surface and internal voids defects

during the welding process can be eliminated by the implementation of the path force controller.

8. Acknowledgement

9. References

[1] Cook, G.E., Crawford, R., Clark, D.E., and Strauss, A.M., 2004, "Robotic Friction Stir Welding," *Industrial Robot*, Vol. 31, No. 1, pp. 55–63.

[2] Smith, C.B., Hinrichs, J.F., and Crusan, W.A., 2003, "Robotic Friction Stir Welding: the State of the Art," *Proceedings of the 4th International Symposium of Friction Stir Welding*, Park City, Utah, May 14–16.

[3] Von Strombeck, A., Schilling, C., and Dos Santos, J.F., 2000, "Robotic Friction Stir Welding – Tool, Technology and Applications," *Proceedings of the 2nd International Symposium of Friction Stir Welding*, Gotherburg, Sweden, June 26–28.

[4] Cook, G.E., Smart, H.B., Mitchell, J.E., Strauss, A.M., and Crawford, R., 2003, "Controlling Robotic Friction Stir Welding," *Welding Journal*, Vol. 82, No. 6, pp. 28–34.

[5] Zhao, X., Kalya, P., and Landers, R.G., 2007, "Empirical Dynamic Modeling of Friction Stir Welding Processes," *ASME International Conference on Manufacturing Science and Engineering*, Atlanta, Georgia, October 15–18.

[6] Åström, K.J. and Wittenmark, B., 1997, *Computer–Controlled Systems–Theory and Design*, 3rd ed., pp. 110–111 and 183–185, Prentice Hall, Upper Saddle River, New Jersey.

[7] De Silva, C.W., 2004, *Mechatronics–An Integrated Approach*, pp. 1032–1034, CRC Press LLC, Boca Raton, Florida.

[8] Ogata, K., 2002, *Modern Control Engineering*, 4th ed., Prentice Hall, Upper Saddle River, New Jersey.

Table 1: Process Parameters and Reference Axial Forces for Axial Force Controller Tracking Experiments.

No.	v (*mm/s*)	ω (*rpm*)	F_{r1} (*kN*)	F_{r2} (*kN*)	F_{r3} (*kN*)
1	3.2	1600	3.45	3.65	3.55
2	3.2	2100	3.25	3.45	3.35
3	2.0	1600	3.00	3.20	3.10
4	2.0	2100	2.70	2.90	2.80
5	2.6	1900	2.90	3.10	3.00

Table 2: Tracking Precision of Steady–State Axial Force (F_1, F_2, and F_3 are the steady–state axial forces for the first, second, and third, respectively, section of the experiment).

No.	$\bar{F}_1 [F_{r1}]$ (*kN*)	$\sigma(F_1)$ (*kN*)	$\bar{F}_2 [F_{r2}]$ (*kN*)	$\sigma(F_2)$ (*kN*)	$\bar{F}_3 [F_{r3}]$ (*kN*)	$\sigma(F_3)$ (*kN*)
1	3.46 [3.45]	$2.75 \cdot 10^{-2}$	3.65 [3.65]	$1.10 \cdot 10^{-2}$	3.54 [3.55]	$2.76 \cdot 10^{-2}$
2	3.27 [3.25]	$1.76 \cdot 10^{-2}$	3.46 [3.45]	$1.84 \cdot 10^{-2}$	3.34 [3.35]	$2.01 \cdot 10^{-2}$
3	3.01 [3.00]	$0.910 \cdot 10^{-2}$	3.21 [3.20]	$1.13 \cdot 10^{-2}$	3.11 [3.10]	$1.36 \cdot 10^{-2}$
4	2.71 [2.70]	$2.15 \cdot 10^{-2}$	2.90 [2.90]	$3.87 \cdot 10^{-2}$	2.80 [2.80]	$1.63 \cdot 10^{-2}$
5	2.92 [2.90]	$2.17 \cdot 10^{-2}$	3.11 [3.10]	$1.33 \cdot 10^{-2}$	3.00 [3.00]	$1.77 \cdot 10^{-2}$

Table 3: Axial Force Tracking Performance for Constant Force Control and Constant Plunge Depth Control in Four-Piece Experiments.

		Constant Axial Force			Constant Plunge Depth		
v (*mm*	ω (*rpm*)	No.	$\bar{F}_1$ (*kN*)	$\sigma(F_1)$ (*kN*)	No.	$\bar{F}_2$ (*kN*)	$\sigma(F_2)$ (*kN*)
3.2	1600	1	3.41	$3.40 \cdot 10^{-2}$	7	3.37	$4.46 \cdot 10^{-2}$
3.2	2100	2	3.31	$3.92 \cdot 10^{-2}$	8	3.55	$6.73 \cdot 10^{-2}$
2.0	1600	3	3.16	$2.90 \cdot 10^{-2}$	9	3.41	$6.06 \cdot 10^{-2}$
2.0	2100	4	2.95	$2.18 \cdot 10^{-2}$	10	3.18	$7.89 \cdot 10^{-2}$
2.6	1900	5	3.25	$3.89 \cdot 10^{-2}$	11	3.12	$5.14 \cdot 10^{-2}$
3.2	2100	6	3.31	$1.69 \cdot 10^{-2}$	12	3.19	$6.85 \cdot 10^{-2}$

Table 4: Tracking Precision of Axial Force Controller in Welding along Constant Gaps.

No.	g (mm)	F_r (kN)	$\bar{F}$ (kN)	$\sigma(F)$ (kN)
1	0.381	3.00	3.01	$1.54 \cdot 10^{-2}$
2	0.762	3.00	3.00	$1.55 \cdot 10^{-2}$
3	0.381–0.762	3.00	3.01	$1.70 \cdot 10^{-2}$
4	0	3.00	3.00	$2.25 \cdot 10^{-2}$

Table 5: Tracking Performance of Path Force Controller during Steady–State (d = 4.20 mm, F_1 and F_2 are the steady–state path forces for the first and second, respectively, section of the experiment).

No.	v (mm/s)	F_{r1} (kN)	$\bar{F}_1$ (kN)	$\sigma(F_1)$ (kN)	F_{r2} (kN)	$\bar{F}_2$ (kN)	$\sigma(F_2)$ (kN)
1	2.0	0.16	0.159	$1.29 \cdot 10^{-2}$	0.13	0.131	$0.727 \cdot 10^{-2}$
2	2.6	0.19	0.191	$1.18 \cdot 10^{-2}$	0.16	0.162	$0.601 \cdot 10^{-2}$
3	3.2	0.23	0.236	$1.34 \cdot 10^{-2}$	0.20	0.202	$0.592 \cdot 10^{-2}$

Table 6: Tracking Performance of Path Force Controller in Weld along a Skin–to–Skin Gap. (d = 4.25 mm and v = 3.2 mm/s, F_1 and F_2 are the steady–state path forces for the first and second, respectively, section of the experiment).

No.	g (mm)	F_{r1} (kN)	$\bar{F}_1$ (kN)	$\sigma(F_1)$ (kN)	F_{r2} (kN)	$\bar{F}_2$ (kN)	$\sigma(F_2)$ (kN)
1	0.381	0.23	0.232	$0.737 \cdot 10^{-2}$	0.20	0.200	$0.838 \cdot 10^{-2}$
2	0.762	0.23	0.228	$0.836 \cdot 10^{-2}$	0.20	0.201	$0.644 \cdot 10^{-2}$
3	0.381–0.762	0.23	0.237	$1.06 \cdot 10^{-2}$	0.20	0.204	$0.636 \cdot 10^{-2}$
3	0	0.23	0.230	$0.861 \cdot 10^{-2}$	0.20	0.202	$0.663 \cdot 10^{-2}$

Figure 1: Friction Stir Welding Operation Schematics for Butt Welding.

Figure 2: Friction Stir Welding System.

Figure 3: FSW Head with Tool and Six–Axis Force/Moment Sensor.
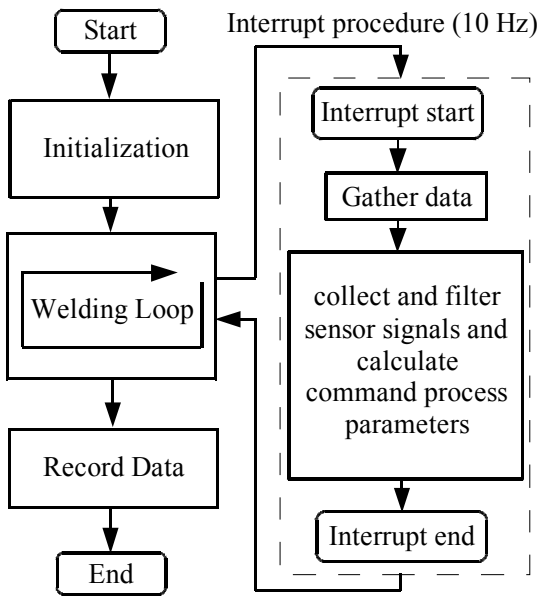
Figure 4: Robotic Friction Stir Welding Force Control Program Functional Block Structure.
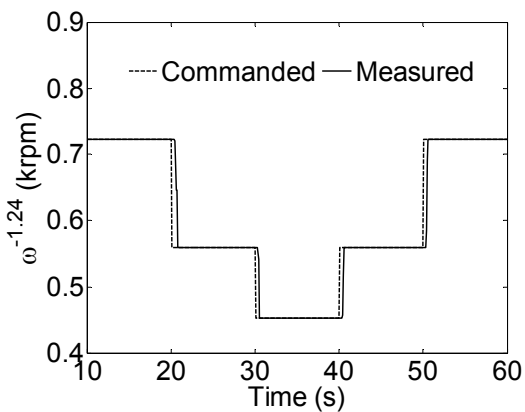
Figure 5: Commanded and Measured Tool Rotation Speed Responses.
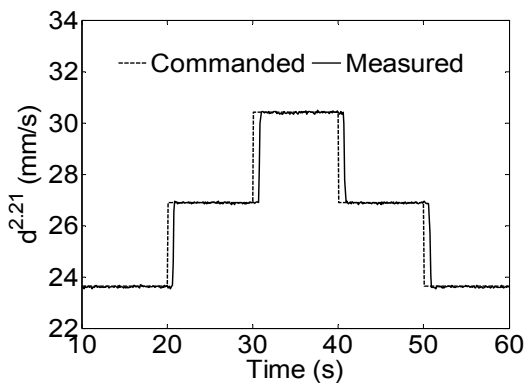
Figure 6: Commanded and Measured Plunge Depth Responses.
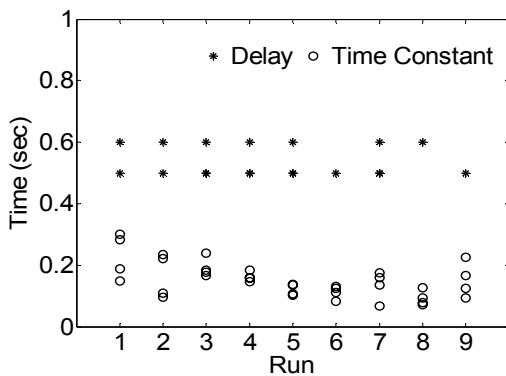
Figure 7: Plunge Depth Equipment Model Delays and Time Constants.
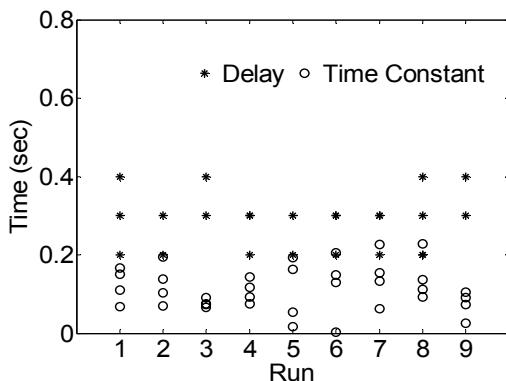
Figure 8: Tool Rotation Speed Equipment Model Delays and Time Constants.
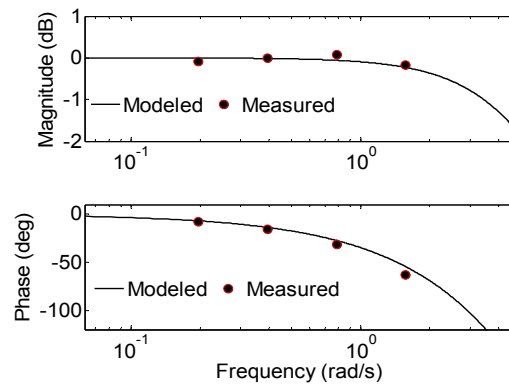
Figure 9: Plunge Depth Equipment Modeled and Measured Bode Diagrams.
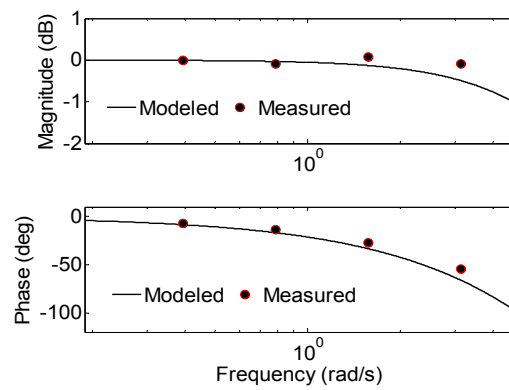
Figure 10: Tool Rotation Speed Equipment Modeled and Measured Bode Diagrams.
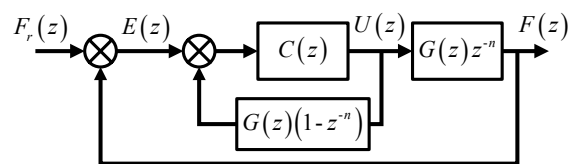
Figure 11: Block Diagram of Closed Loop Control System.
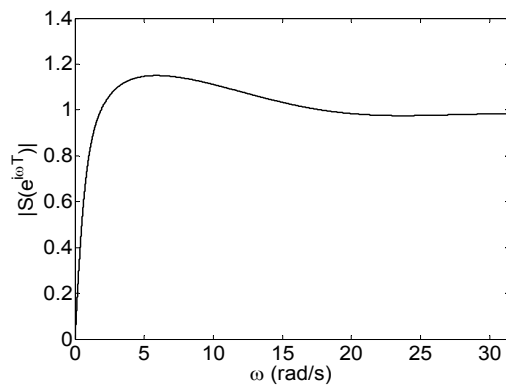
Figure 12: Axial Force Closed Loop System Sensitivity Function.
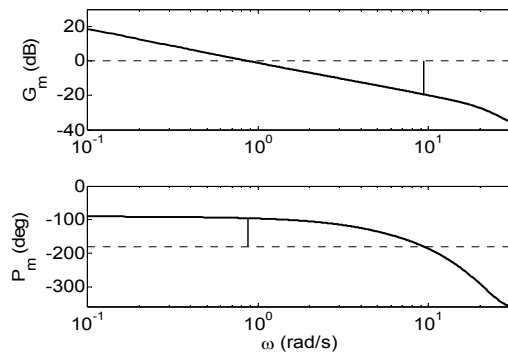
Figure 13: Axial Force System Bode Diagram and Stability Margins.

(G_m = 19.4 dB and P_m = 84.4°).
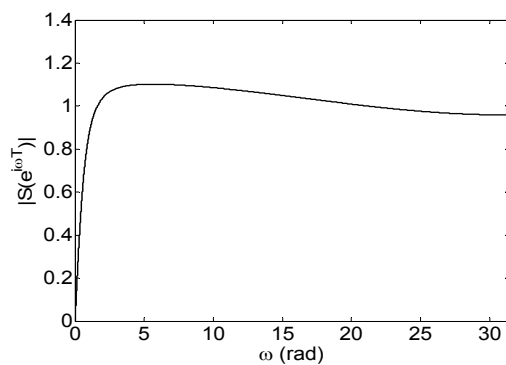
Figure 14: Path Force Closed Loop System Sensitivity Function.
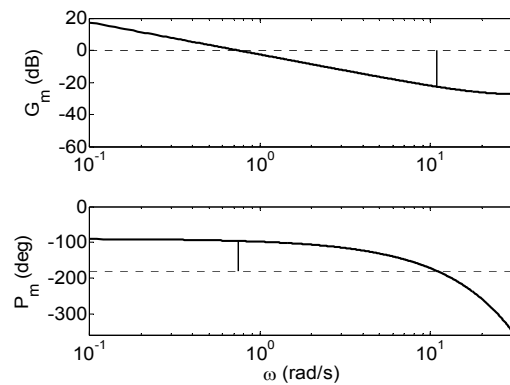
Figure 15: Path Force System Bode Diagrams and Stability Margins.

(G_m = 22.6 dB and P_m = 83.9°).

Figure 16: Lap Welding Experimental Setup.
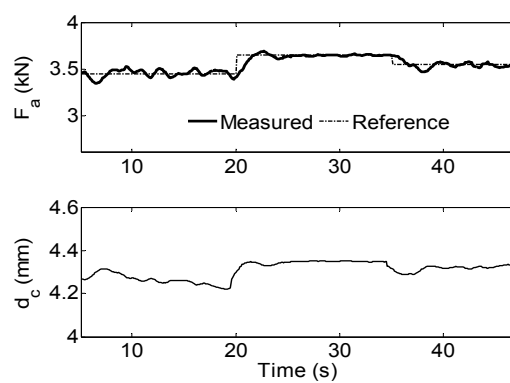
Figure 17: Experimental Results for Step Changes in Reference Axial Force

(v = 3.2 *mm/s* and ω = 1600 *rpm*).
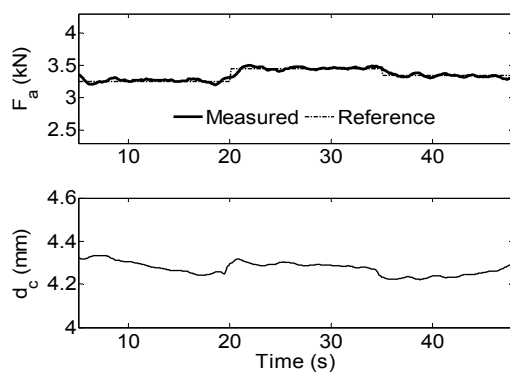
Figure 18: Experimental Results for Step Changes in Reference Axial Force

(*v* = 3.2 *mm/s*, *ω* = 2100 *rpm*).
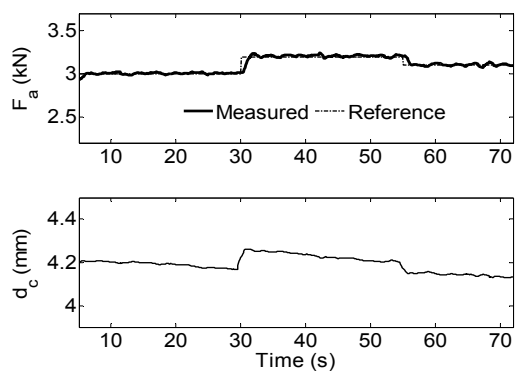
Figure 19: Experimental Results for Step Changes in Reference Axial Force

(*v* = 2.0 *mm/s*, *ω* = 1600 *rpm*).
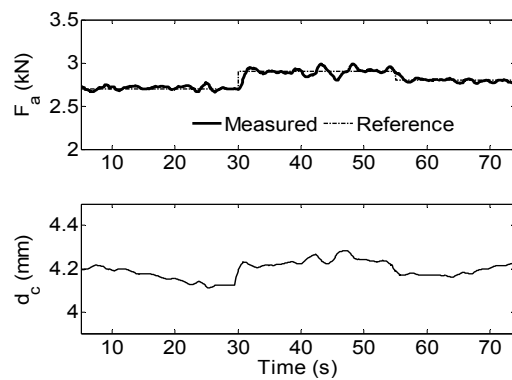
Figure 20: Experimental Results for Step Changes in Reference Axial Force

($v = 2.0$ *mm/s*, $\omega = 2100$ *rpm*).
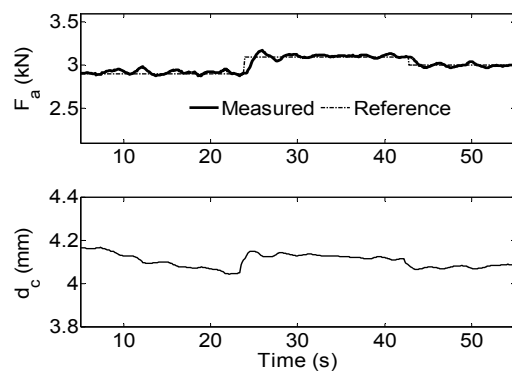
Figure 21: Experimental Results for Step Changes in Reference Axial Force

($v = 2.6$ *mm/s*, $\omega = 1900$ *rpm*).
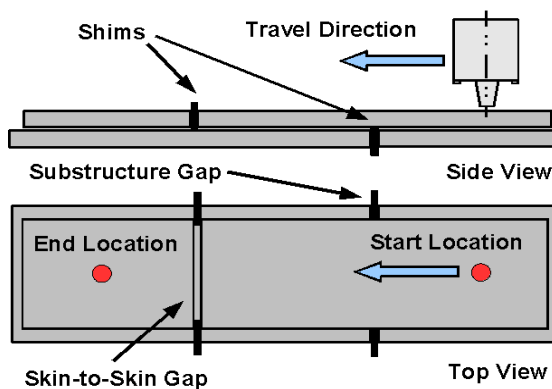
Figure 22: Four–Piece Lap Welding Experimental Setup with Substructure and Skin–to–Skin Gaps.
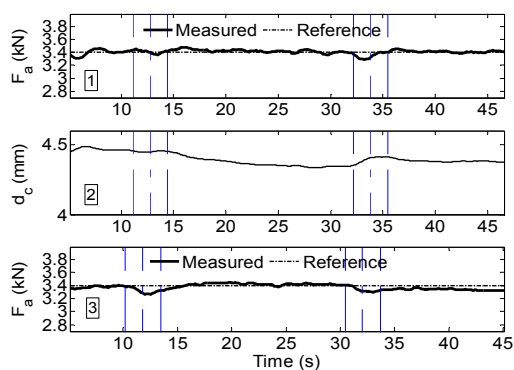

Figure 23: Four–Piece Experimental Results (#1 and #7) for Force Control and Constant Plunge Depth Control. (F_r = 3.4 kN, d = 4.28 mm, v = 3.2 mm/s, ω = 1600 rpm, and g = 0.381 mm).
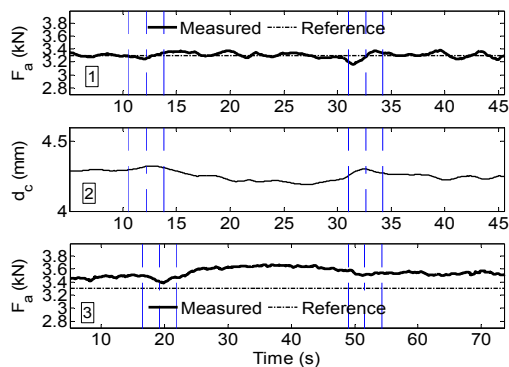
Figure 24: Four–Piece Experimental Results (#2 and #8) for Force Control and Constant Plunge Depth Control. (F_r = 3.3 *kN*, d = 4.20 *mm*, v = 3.2 *mm/s*, ω = 2100 *rpm*, and g = 0.381 *mm*).
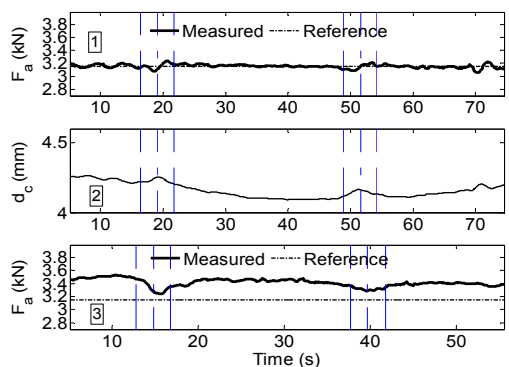
Figure 25: Four–Piece Experimental Results (#3 and #9) for Force Control and Constant Plunge Depth Control. (F_r = 3.15 *kN*, d = 4.21 *mm*, v = 2.0 *mm/s*, ω = 1600 *rpm*, and g = 0.381 *mm*).
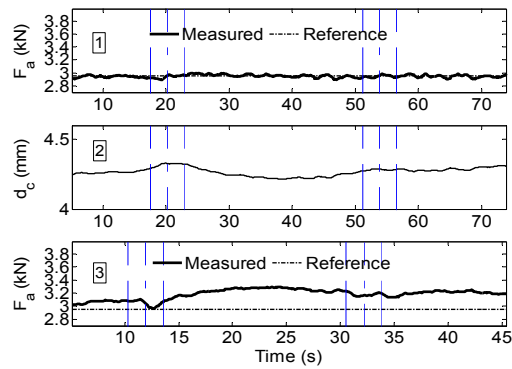
Figure 26: Four–Piece Experimental Results (#4 and #10) for Force Control and Constant Plunge Depth Control. (F_r = 2.95 *kN*, d = 4.20 *mm*, v = 2.0 *mm/s*, ω = 2100 *rpm*, and g = 0.381 *mm*).
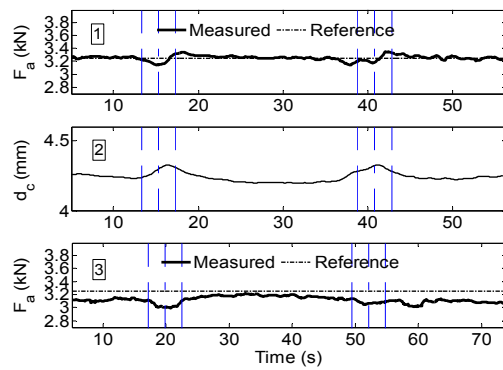
Figure 27: Four–Piece Experimental Results (#5 and #11) for Force Control and Constant Plunge Depth Control. (F_r = 3.25 *kN*, d = 4.25 *mm*, v = 2.6 *mm/s*, ω = 1900 *rpm*, and g = 0.381 *mm*).
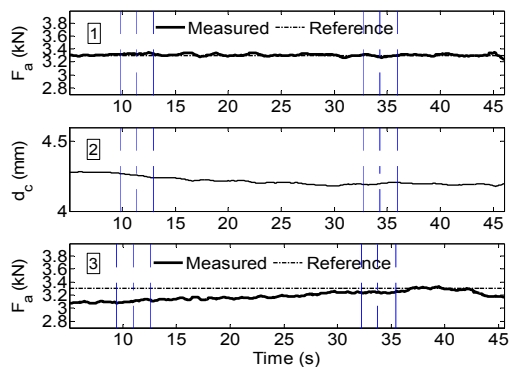
Figure 28: Four–Piece Experimental Results (#6 and #12) for Force Control and Constant Plunge Depth Control. (F_r = 3.3 *kN*, *d* = 4.25 *mm*, *v* = 2.6 *mm/s*, ω = 1900 *rpm*, and *g* = 0 *mm*).
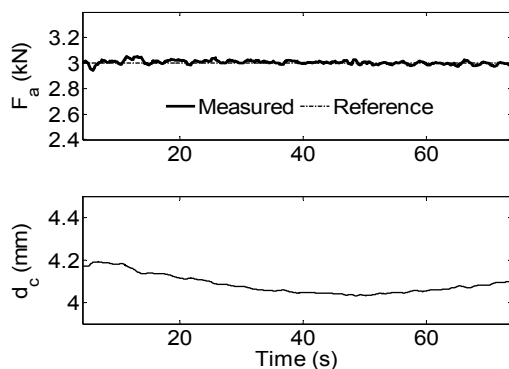
Figure 29: Axial Force Along a Gap and Plunge Depth with the Implementation of Axial Force Controller (*g* = 0.381 *mm*).
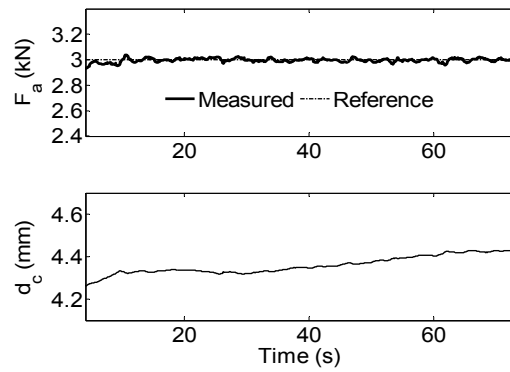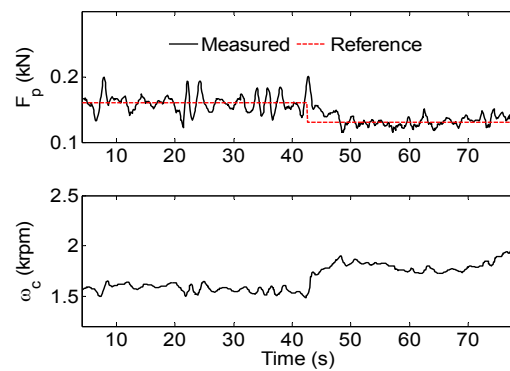
Figure 30: Axial Force Along a Gap and Plunge Depth with the Implementation of Axial Force Controller ($g = 0.762$ *mm*).
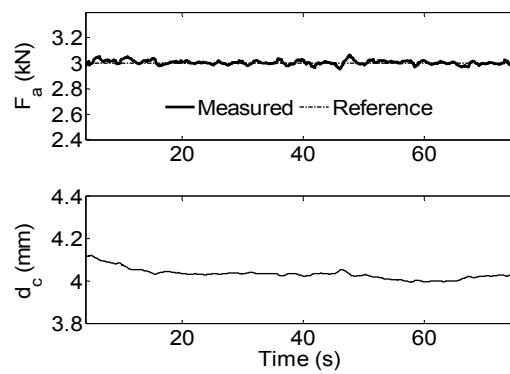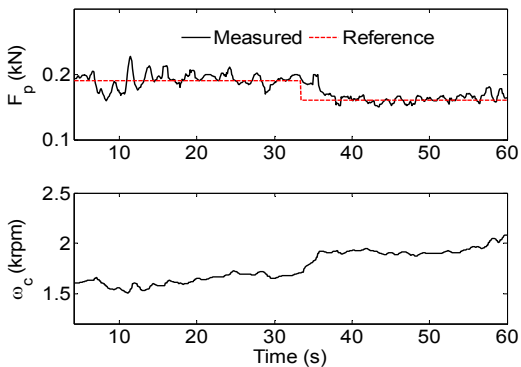

Figure 31: Axial Force Along a Gap and Plunge Depth with the Implementation of Axial Force Controller (tapered gap, $g = 0.381–0.762$ *mm*).
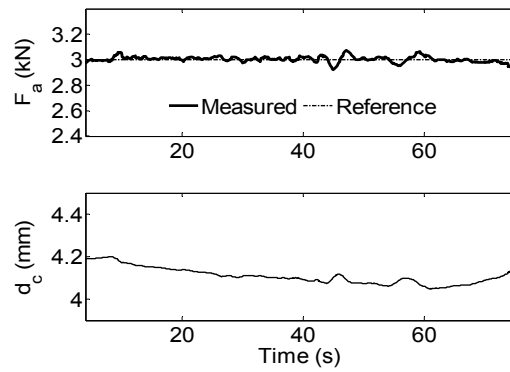
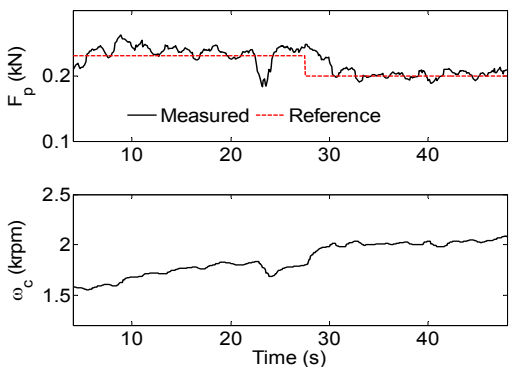**Figure 32: Axial Force Along a Gap and Plunge Depth with the Implementation of Axial**

Force Controller (*g* = 0 *mm*).

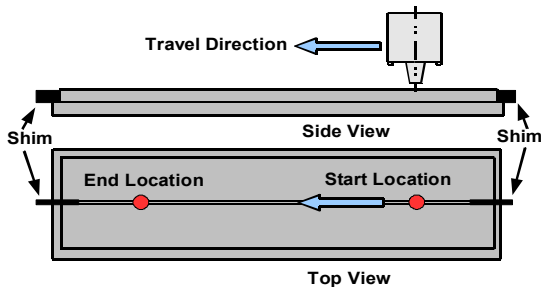**Figure 33: Path Force and Tool Rotation Speed for Path Force Controller (*d* = 4.20 *mm***
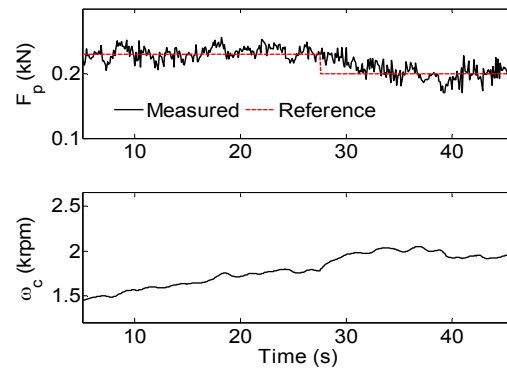
and *v* = 2.0 *mm/s*).

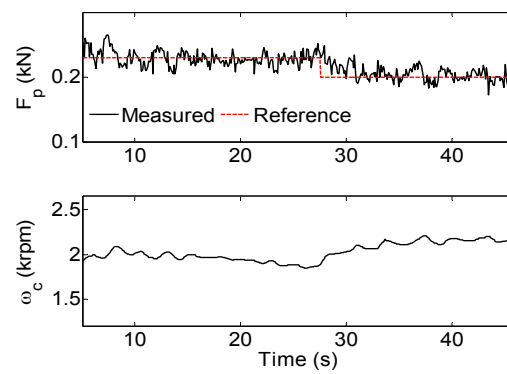**Figure 34: Path Force and Tool Rotation Speed for Path Force Controller (*d* = 4.20 *mm* and *v* = 2.6 *mm/s*).**

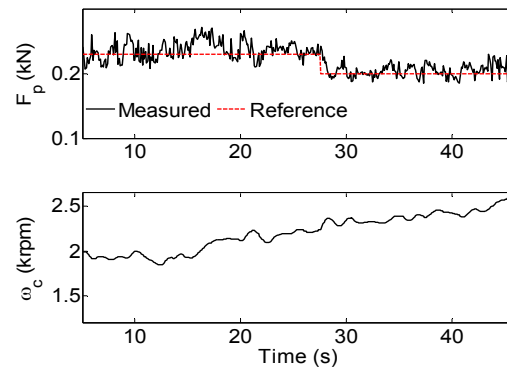**Figure 35: Path Force and Tool Rotation Speed for Path Force Controller (*d* = 4.20 *mm* and *v* = 3.2 *mm/s*).**

Figure: 36: Path Force Along a Gap Experimental Setup.

Figure: 37: Path Force Along a Gap and Tool Rotation Speed with the Implementation of

Path Force Controller (*g* = 0.381 *mm*).

Figure 38: Path Force Along a Gap and Tool Rotation Speed with the Implementation of

Path Force Controller (*g* = 0.762 *mm*).

Figure 39: Path Force Along a Gap and Tool Rotation Speed with the Implementation of Path Force Controller (tapered gap, *g* = 0.381–0.762 *mm*).
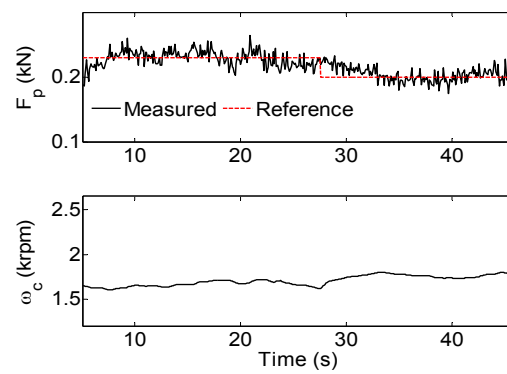

Figure 40: Path Force Along a Gap and Tool Rotation Speed with the Implementation of Path Force Controller (*g* = 0 *mm*).

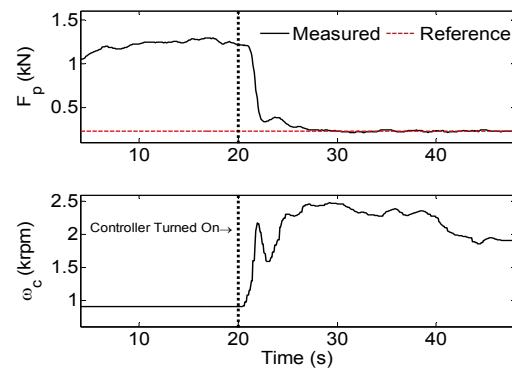**Figure 41: Path Force Before and After the Controller Implementation.**

(*v* = 3.2 *mm/s*, *d*= 4.20 *mm*).

Figure 42: Nugget Cross Sections with (a) Path Force Control and (b) without Path Force

Control. (*v* = 3.2 *mm/s*, *d*= 4.20 *mm*).

SECTION

2. SUMMARY, CONCLUSIONS AND FUTURE WORK

The process variables (i.e., axial, path, and normal forces) in a FSW process were dynamically modeled as functions of the process parameters (i.e., plunge depth, travel speed, and rotation speed). As presented in the first paper of this thesis, the modeling procedure consisted of two steps: static modeling using the Least Squares method and dynamic modeling using the Recursive Least Squares method. The experimental results indicate that the axial force is primarily affected by the plunge depth and may be modeled as a second order dynamic process with two real poles and the path force is primarily affected by the travel speed and rotation speed and may be modeled as a first order process. The normal force is affected by all three process parameters and may also be modeled as a first order process. It is believed the dynamic response of the forces is also affected by the mechanical and thermal processes, as well as the machine's dynamic structural characteristics. The static axial force model has a very good correlation coefficient, but the static path and normal force models have relatively poor correlation coefficients, which could be due to the chaotic behavior of the stirring process, as compared to the forging process, and the smaller signal to noise ratio. Various validation experiments were conducted and validated the developed models.

Based on the developed models, nonlinear axial and path force controllers were designed using the Polynomial Pole Placement technique with the Internal Model Principle and the controllers were implemented in a Smith–Predictor–Corrector structure to compensate for the inherent equipment delay. Validation experiments show that the

axial force controller works well in tracking constant forces despite the presence of gaps both along and across the weld path. Also, the path force controller is able to track a constant force in the presence of a gap along the weld path. The path force controller has a relatively lower tracking precision compared to the axial force controller, which is believed to be a result of both smaller signal to noise ratio and the modeling inaccuracies in the path force model. One validation experiment shows that defects such as surface and internal voids can be eliminated by the implementation of the path force controller.

Although the dynamics of FSW process variables can be well characterized by simple first or second order system models, the modeling work is not completed in that 1) the underlying mechanisms and physical explanations are still not clear; and 2) the path and normal force models contains relatively more inaccuracies compared to the axial force model, which could be reduced by improving the sensor's signal conditioning module of the experimental system and reducing the variations of experimental setup conditions, such as fixturing, thermo-mechanical boundary conditions, and the plate machining error. Consequently, the path force controller performance is significantly influenced by the path model inaccuracies and the force dynamic response uncertainties. One possible solution to this problem in the future is to design and implement an adaptive controller, which can perform online estimations of the process dynamics and update controller coefficients. Currently, the axial and path force controllers are implemented independently. Another future work is to investigate the Multi–Input–Multi–Output system where both of them are implemented simultaneously during the weld and therefore, to regulate the axial and path forces at the same time.

VITA

Xin Zhao was born on July 17th, 1978 in Beijing, a city in the northern part of China. He went to the Department of Precision Instrument, Tsinghua University for his undergraduate studies and received his Bachelor degree in Mechanical Engineering in August 2001. He worked for Kaitian Tech Inc. at Beijing from 2001 to 2005 as an engineer before he went to U.S. for an advanced degree. He joined the master program in the Department of Mechanical and Aerospace Engineering of the University of Missouri–Rolla and received his M.S. degree in Mechanical Engineering in December 2007. His topics of interest include the dynamic modeling and control of Friction Stir Welding processes. After graduation, he will work as a systems engineer in Cummins Inc., at Columbus, Indiana.